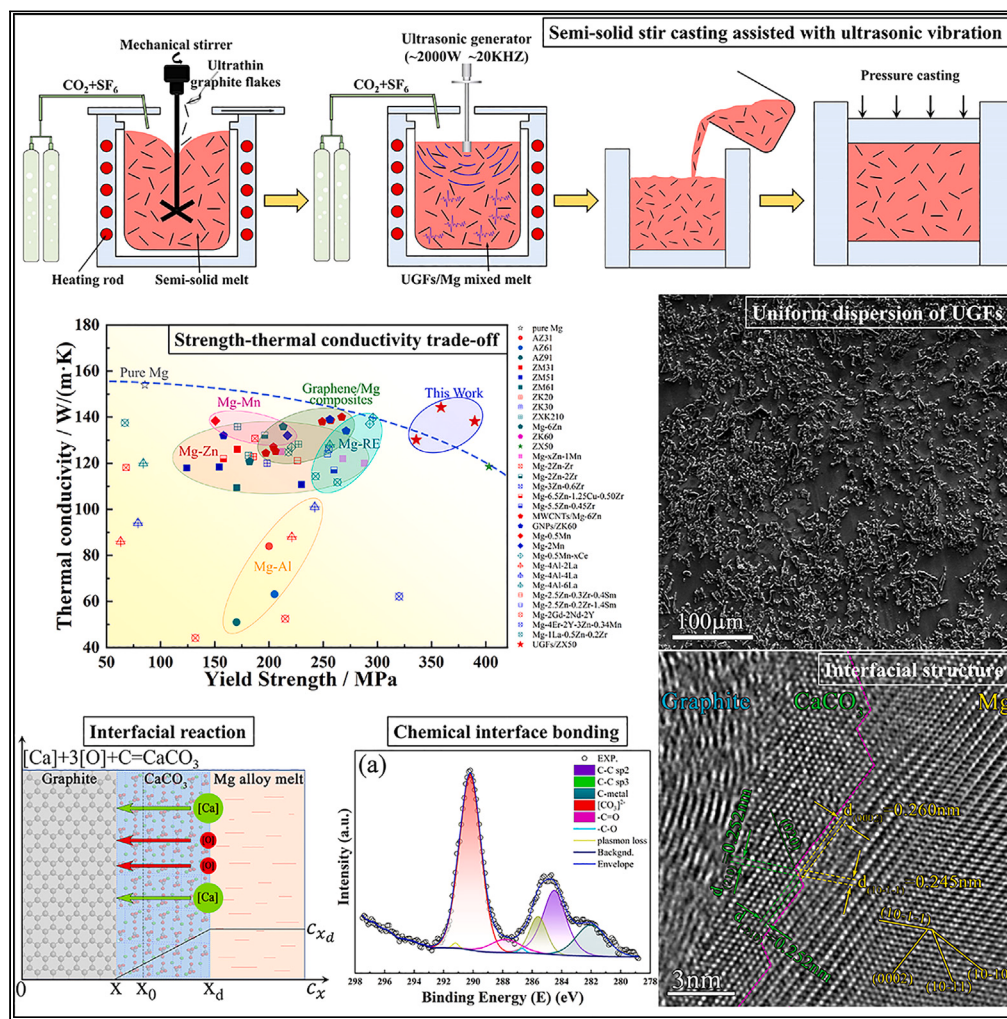


Article

Thermal conductivity and mechanical properties of graphite/Mg composite with a super-nano CaCO_3 interfacial layer

Li Zhang, Kun-kun Deng, Kai-bo Nie, ..., Quan-xin Shi, Yu Liu, Jie Wang

dengkunkun@tyut.edu.cn (K.-k.D.)
xuchao_hit@163.com (C.X.)
wjie_no1@sjtu.edu.cn (J.W.)

Highlights

A super-nano CaCO_3 interfacial layer was developed in carbon/Mg system

Several preferential epitaxial relationships exist between Mg and CaCO_3

Strong ionic bond of graphite/ CaCO_3 interface was demonstrated

Interfacial strengthening endows the composites with superior properties



Article

Thermal conductivity and mechanical properties of graphite/Mg composite with a super-nano CaCO₃ interfacial layer

Li Zhang,^{1,2} Kun-kun Deng,^{1,5,*} Kai-bo Nie,¹ Cui-ju Wang,¹ Chao Xu,^{3,*} Quan-xin Shi,¹ Yu Liu,¹ and Jie Wang^{4,*}

SUMMARY

Incorporating graphite/graphene into a Mg alloy matrix is a promising approach for developing lightweight heat dissipation materials. However, carbon material is inherently incompatible with Mg because of their distinctly different surface characteristics, resulting in the challenge of composite fabricating and interface controlling. Herein, a new strategy of *in situ* interfacial modification was proposed to achieve excellent thermal conductivity and mechanical properties in graphite/Mg composites. A super-nano CaCO₃ interfacial layer was reported in this paper. The detailed interfacial structure, reaction thermodynamics and kinetics, and interface strengthening mechanisms were analyzed and discussed. Several preferential epitaxial relationships of the Mg/CaCO₃ interface were revealed, which are conducive to minimize the interfacial energy, stabilize and strengthen the interface. Moreover, strong ionic bond of graphite/CaCO₃ interface was demonstrated. The strong chemical interface bonding of graphite-Mg via *in situ* interface modification facilitates both the interfacial cohesion and interfacial thermal conduction, which endows the graphite/Mg composites with superior strength-thermal conductivity synergy.

INTRODUCTION

The rapid development of modern miniaturizing electronic devices, such as high-frequency integrated circuit, high energy density fast-charge battery, and high-power light-emitting diode (LED) lighting device, brings a wide adoption of lightweight high thermal conductivity material. Magnesium alloy is the lightest structural metallic material.^{1–3} Also, more exciting is that the thermal conductivity of magnesium is top-ranking among numerous metallic materials, let alone other nonmetal lightweight materials such as wood, ceramics, and polymers.^{4–8} It is foreseeable that magnesium takes an advantageous position in the area of lightweight high thermal conductivity materials.

In general, alloying design and microstructure control were usually applied to pursue high thermal conductivity but often at the sacrifice of the strength of the alloy. High thermal conductivity requires a perfect crystal for the movement of phonons/electrons.^{2,3,9,10} Whereas, high strength requires obstacles like solute atoms, grain boundaries and precipitates to hinder the movement of dislocations. These two mutually exclusive properties pose the challenge of alloy design and properties trade-off. For example, as-extruded commercial Mg alloy AZ91 shows respectable strength of ~300 MPa¹¹ but offers low thermal conductivity of ~46.9 W/(m·K).³ On the contrary, thermal conductivity of pure Mg is 156 W/(m·K) but accompanied with a very low strength,^{3,12} which limits it from being widely adopted by industry. The wide industry adoption of Mg heat-dissipation alloys should meet the demands of both mechanical and thermal conductivity, in cases like the shells of electronic products and the heat management structure of vehicles.

A promising approach to overcome the strength-thermal conductivity dilemma is incorporating high thermal conductive reinforcements into a Mg alloy matrix. Graphite flakes are a candidate for their high thermal conductivity (~800–2000 W/(m·K)) and high elastic modulus (~800 GPa) along the crystallographic basal plane.^{13–16} Phase interface is unambiguously a key component in composite materials, because the bulk properties of graphite/Mg composites are critically determined by their interfacial characteristics. Unfortunately, graphite is inherently incompatible with Mg because of their distinctively different surface

¹Shanxi Key Laboratory of Advanced Magnesium-based Materials, College of Materials Science and Engineering, Taiyuan University of Technology, Taiyuan 030024, China

²Teaching Center of Experiment and Practice, Shanxi Datong University, Datong 037000, China

³School of Materials Science and Engineering, Harbin Institute of Technology, Harbin 150001, China

⁴National Engineering Research Center of Light Alloy Net Forming, Shanghai Jiao Tong University, Shanghai 200240, China

⁵Lead contact

*Correspondence:
[\(K.-k.D.\),
\[\\(C.X.\\),
\\[\\\(J.W.\\\)\\]\\(mailto:wjie_no1@sjtu.edu.cn\\)\]\(mailto:xuchao_hit@163.com\)](mailto:dengkunkun@tyut.edu.cn)

<https://doi.org/10.1016/j.isci.2023.106505>



characteristics. Graphite shows poor wettability with molten Mg, owing to their big difference in surface energy.¹⁷ Such bonding is theoretically considered to be weak. Interface microstructural characteristics, such as purity, compositions, orientations, defects, and strain at or in the vicinity of interfaces, govern the wettability, interface bonding strength, interface thermal resistance, and even dispersibility of graphite flakes,¹⁷ which further exert enormous influences on the composite's physical and mechanical properties.

Strategies toward interfacial modification have been put forward to help relieve the poor compatibility of graphite with metals.¹⁷ The *in situ* formation of Al₄C₃ compound has been reported at the interface of graphene/Al composites when the temperature exceeds 650°C.¹⁸ Besides, the matrix alloying method in Graphene/Cu composites has also been explored. With the addition of strong carbide-forming elements such as Ti, Cr, B, and Zr that can react with carbon, an interfacial carbide layer can be formed.¹⁹ Another interface modifying path usually picked by graphite/Cu composites is coating graphite with Ni, B₄C, SiC, and Cr₇C₃ by salt bath or electroless deposition method.^{20–24} However, few effects have been achieved for the purpose of thermal conductive enhancement as the interface layer is difficult to be controlled and much thicker than expected; for instance: Ni coating ~ 3–8 μm,²² B₄C coating ~0.35 μm,²³ SiC coating ~0.25–0.3 μm,^{20,21} and Cr₇C₃ coating ~0.52–0.95 μm.²⁴

Interface modification could be even more challenging for a graphite-Mg system. The current experiences on Cu and Al matrix composites may not be applicable because of the much higher chemical activity of Mg. To the best of our knowledge, no effective methods have been proposed so far for control of the graphite-Mg interfacial reaction. Some researchers believe the formation of MgO could improve wettability and bonding of graphite-Mg interface.^{25–28} But that cannot be strictly considered as interfacial reaction, since the graphite does not involve into reaction. In addition, the spherical and hemispheric MgO can hardly be spread at the graphite surface.^{25–28} As a result, the quality of MgO layer cannot be controlled; it may form at the graphite-Mg interface or in the vicinity of graphite.^{25–28} The interface modification for thermal conductive application is very complicated; there are a lot of quality problems that need to be controlled, including the byproduct, purity, cover area, homogeneousness and compactness, and bonding strength with graphite.

Interface defects introduce additional phonon scattering, causing increased interfacial heat resistance.^{1,3} Hence, the fabricating techniques for graphite/Mg composites need to be elaborately designed. For now, the adaptable manufacturing techniques for large-scale industrialization are stir-casting, powder sintering, and additive manufacturing. Powder sintering and additive manufacturing are suitable for good dispersion of graphite, but inherent pores, interstices, and impurities are difficult to prevent.^{29,30} Unfortunately, the defects and impurities in metal matrix or at the interface are all vitally harmful to thermal conductivity.^{31,32} Second, the sintering of Mg powders is very dangerous, because magnesium is combustible and explosive.^{33,34} Moreover, powder blending techniques such as ball milling usually introduce new impurities³² and break the graphite flakes.³⁵

Comparatively, the solidification processing of casted magnesium matrix composites has already demonstrated its feasibility of eliminating pores, controlling impurities, and dispersing reinforcements.³⁶ Therefore, the semi-solid stir casting assisted with ultrasonic vibration was adopted in this work, due to the advantages of stir-casting can be most employed by proper technological parameter control. We conclude the following guidelines on the alloy design and fabrication.

- (1) The ultrathin graphite flakes (UGFs) with average thickness of ~0.1 μm and lateral size of ~2.0 μm, which is considered as a proper size. It was reported that the surface energy barrier (ΔE) of ceramic particle rapidly increases with the size decreases.³⁶ The excessively smaller graphite, e.g., the graphene nanoplatelets (GNPs), is not appropriate for huge dispersive resistance. Moreover, the graphene with several atomic layers is prone to being completely consumed by the chemical reaction. The thermal conductivity of graphite mainly depends on the orientation and graphitization. The 3D highly oriented pyrolytic graphite (HOPG) holds the thermal conductivity record of ~2000 W/(m·K) at 300 K, comparable with graphene.¹³ On the other side, large size graphite flakes are also disfavored for the declining mechanical and thermal conductive properties.^{15,16}
- (2) During the mechanical stirring, the large pressure difference and shear forces of solid-liquid mixed melts can efficiently entrap and suck the UGFs into the vortex. On the other side, the vigorously stirred semi-solid melts also contribute to wiping the graphite surface to make it cleaner, which

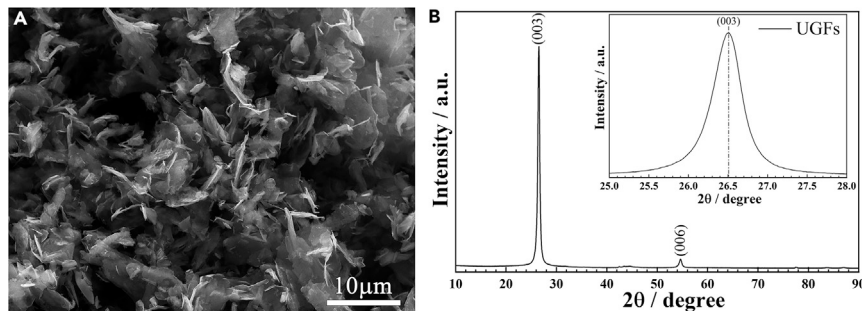


Figure 1. Morphology and structure characterization of raw UGFs

(A) Scanning electron microscope image showing the morphology of raw UGFs.
(B) XRD pattern of raw UGFs.

would benefit the wettability.³⁷ Moreover, the high temperature Mg alloy melt during stir-casting process builds a stunning platform for the *in situ* interfacial reaction, for its homogeneous chemical component and fast element transfer.

- (3) High energy ultrasonic processing (~2000 W) conducted on the UGFs/Mg melt mixture ensures the uniform distribution of the UGFs. References have confirmed that the acoustic streaming accompanied by transient cavitation, micro-hot and high-pressure spots can potentially clean the UGFs surface, break the UGFs clusters, and promote degasification.³⁸
- (4) The alloying component design of Mg matrix: Mg-5Zn-0.5Ca (wt %), named ZX50 hereafter. The addition of 5% Zn insures a large semi-solid window. Besides, Zn has less negative effect on thermal conduction of Mg matrix compared with other alloying elements such as Al and Sn.³⁹ The additional upsides from Zn element are the improved mechanical properties, including improved non-basal slip activities by reducing critical resolved shear stress (CRSS) anisotropy and enhanced ductility, solution and precipitation strengthening effects.⁴⁰ The addition of 0.5% Ca aims to prevent burning and anti-oxidation during melting and casting processes.³³ The grain refinement effect of Ca is also desired for the high strength requirement.⁴¹ Also, other benefits to mechanical properties include higher dislocation binding energy, promotion of pyramidal $\langle a \rangle$ slip and basal-to-prismatic cross-slip, and solution and precipitation strengthening effects.⁴⁰ Moreover, Ca element with high chemical activity which readily donates its s-electrons brings us an unexpected interfacial reaction:
$$[Ca]_{0.5\%} + C_{(s)} + 3[O] = CaCO_3{}_{(s)} \Delta G^\circ_{680^\circ C} = -684.19 \text{ kJ/mol.}$$
- (5) Benefits from the interfacial reaction, such as: it reduces the surface energy difference, facilitates the wetting between graphite and Mg alloy melt, eliminates the amorphous carbon and adsorbed oxygen at the graphite surface, and strengthens the interface bonding, et al.^{17,19,36,37}

Based on the design strategy mentioned above, the graphite/Mg composite with excellent thermal conductivity and mechanical properties was developed in this work. The interfacial structure, forming thermodynamics and kinetics mechanism, and their effects on mechanical and thermal conductive properties have been analyzed and discussed. To the best of our knowledge, such *in situ* interface modification methodology has not been reported in carbon/magnesium composites, even for other carbon/metal systems. We believe this work could provide inspiration for future research and practical applications.

RESULTS AND DISCUSSION

Microstructure

Figure 1A shows the scanning electron microscope (SEM) morphology of raw UGFs. Figure 1B shows the XRD (X-ray diffraction) pattern of the UGFs. There are two peaks at the 2θ value of $\sim 26.5^\circ$ and $\sim 54.6^\circ$, which are associated with the crystal planes of (003) and (006), respectively. No other peaks were identified by the XRD result, indicating the high purity of UGFs. The graphitization degree of UGFs was calculated as 93.6% from the XRD spectra using Maire-Mering model.⁴²

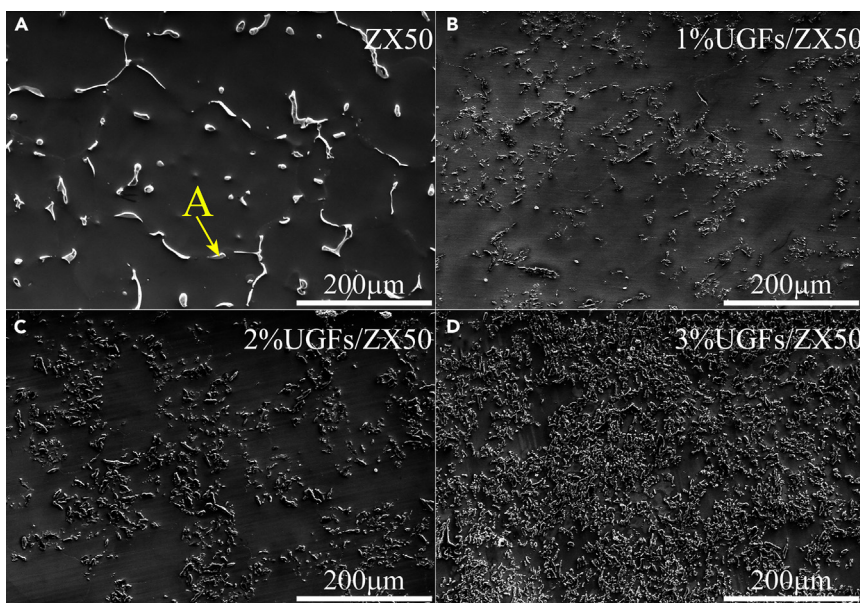


Figure 2. SEM micrographs of as-cast ZX50 alloy and UGFs/ZX50 composites

(A) ZX50 alloy, the dark continuous phase is α -Mg, the bright dispersed phases are intermetallic; (B) (C) and (D) 1, 2, and 3 vol % UGFs/ZX50 composite, the dark continuous phase is α -Mg, the rod-like phases with bright edges are UGFs.

The SEM microstructure images of the as-cast materials are shown in Figure 2. The microstructure of ZX50 alloy depicted in Figure 2A comprises primary α -Mg phase with black contrast and eutectic phase with white contrast. The composition of the eutectic phase was determined by energy-dispersive X-ray spectroscopy (EDS) analysis (point A in Figure 2A) with 63.4 Mg-33.0Zn-2.54Ca (at.%), which indicates a kind of Mg-Zn phase. Figures 2B–2D are SEM microstructure images of UGFs/ZX50 composites with UGFs volume fraction of 1%, 2%, and 3%, respectively. As can be seen, the UGFs of 1% UGFs/ZX50 are usually dispersed in the inter-dendritic region. This phenomenon results from the interaction between UGFs and solidifying interface during solidification. After the suspension of UGFs in melts is poured into molds, the metal starts to solidify while the UGFs move under the influence of normal gravity and solidifying process. It is reported that reinforcements are frequently pushed into last solidifying inter-dendritic regions by advancing dendritic interfaces, because their thermal diffusivity is lower than that of the matrix.³⁶ With the UGFs content increasing, the UGFs' distribution range extends to the inner dendrite, and becomes more homogeneous. This means that the UGFs are easier engulfed rather than pushed by solidifying interfaces, especially for the higher volume fraction of UGFs. The good UGFs macroscopic distribution may partly be ascribed to the interfacial reaction that contributes to the alleviation of the surface energy difference and facilitated wettability.¹⁷ Moreover, other factors also account for this phenomenon such as: (1) The high thermal conductivity and low curvature of UGFs make it easier to be engulfed by solidifying interfaces; (2) the introduction of more UGFs speeds up the heat transportation, leading to a larger undercooling of slurry, promoting the nucleation and growth of dendrites, (3) the higher viscosity caused by the larger content of UGFs makes it easier to be engulfed by solidifying interfaces as well.³⁶

The optical microscopy (OM) and SEM micrographs of the as-extruded ZX50 alloy and UGFs/ZX50 composites are shown in Figure 3. The microstructures comprise fine equiaxed dynamic recrystallized (DRXed) grains, elongated unDRXed grains, and UGFs. The average grain size (d) and volume fraction (VF_{DRX}) of DRXed grains of ZX50 alloy were measured as $\sim 0.27 \mu\text{m}$ and 47.9%, respectively. The addition of UGFs leads to increased grain size and VF_{DRX} which may be explained as the consumption of Ca, the promoted DRX nucleation, and more generated heat energy⁴³ caused by plastic strain coordination. Moreover, it can be seen in Figure 3 that the UGFs are rotated and aligned along the extrusion direction in the Mg matrix.

Figure 4 shows the high angle annular dark field (HAADF) image and the corresponding selected area electron diffraction (SAED) pattern of the as-extruded 2 vol % UGFs/ZX50 composite. The UGFs with lamellar

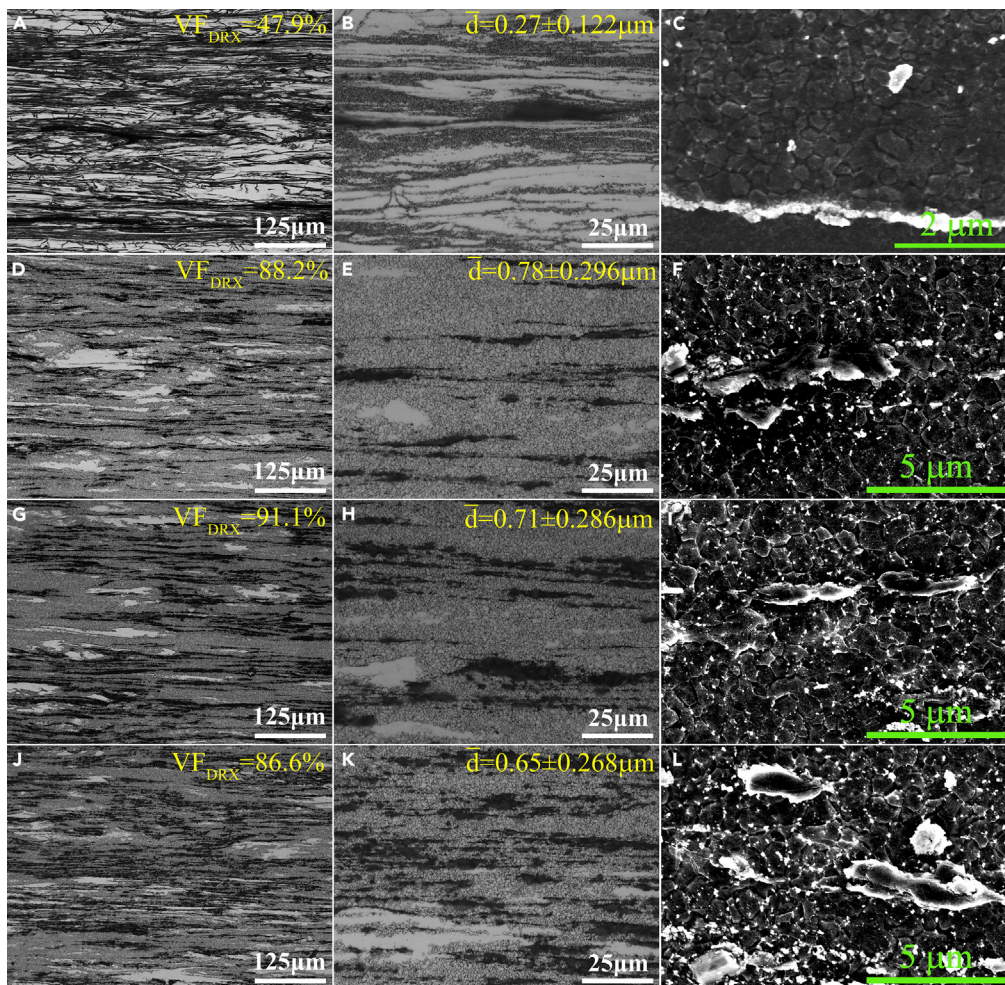


Figure 3. OM and SEM micrographs of as-extruded ZX50 alloy and UGFs/ZX50 composites

(A–C) ZX50 alloy.

(D–F) 1% UGFs/ZX50 composite.

(G–I) 2% UGFs/ZX50 composite.

(J–L) 3% UGFs/ZX50 composite. The rod-like phases with bright edges shown in (F) (I) (L) are UGFs, whereas the bright phase with a long ribbon shape shown in (C) is $\text{Ca}_2\text{Mg}_6\text{Zn}_3$. The bright nano-scale spherical phases in figure (C, F, I, L) are MgZn_2 precipitations.

structure in Figure 4A are distributed with parallel orientation and alignment. The corresponding element mapping images indicate that the Ca and O elements were segregated with the graphite. This indicates that substances may consist of Ca or/and C or/and O elements. The SAED analysis in Figure 4B demonstrates that the flake at point A in Figure 4A is graphite.

As depicted in the SEM images in Figure 3, a large amount of fine spherical precipitates distributed dispersedly within the grain interiors and at grain boundaries. The HAADF-STEM (scanning transmission electron microscopy) and corresponding element mapping images in Figure 4 confirmed that Zn and Mg are major elements of the spherical precipitates. Combined with the XRD profiles shown in Figure 5A, the precipitates were identified as MgZn_2 . The diffraction peaks at 2θ value of $\sim 26.5^\circ$ indicate the existence of UGFs and the peak intensity correlates with the volume fraction of UGFs. The Raman spectra of the raw UGFs and the 3% UGFs/ZX50 composite are shown in Figure 5B. There are three common peaks located at the 1350 cm^{-1} , 1580 cm^{-1} and 2700 cm^{-1} Raman shift, corresponding to the D peak, G peak and 2D peak, respectively.⁴⁴ The decreased I_D/I_G value indicates the decreased disorder. The redshift of the peaks may result from charge transfer and strain effect.⁴⁵

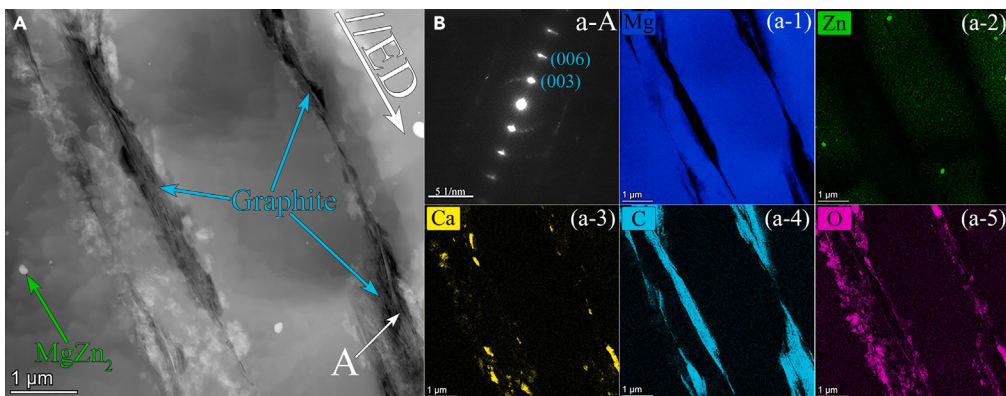


Figure 4. Transmission electron microscope (TEM) analysis of the as-extruded UGFs/ZX50 composite

(A) High angle annular dark field (HAADF) image and corresponding elements mappings images. The nano-scale spherical phase marked by green arrow is MgZn_2 . The flakes marked by blue arrows are graphite which coincide with the element distribution.

(B) Selected area electron diffraction (SAED) pattern of graphite in (a) marked as point A.

Mechanical property and thermal conductivity

The tensile stress-strain curves of the as-extruded ZX50 alloy and UGFs/ZX50 composites are shown in Figure 6. The yield strength (YS) and elongation of ZX50 alloy are ~ 410.2 MPa and $\sim 4.04\%$, respectively. The YS was decreased whereas the elongation was increased with the induction of UGFs. The decreased YS mainly results from the distinct increase of grain size. As shown in Figure 3, the average grain size of ZX50 alloy is measured as ~ 0.27 μm . Comparatively, the average grain size of UGFs/ZX50 composites is about 2.6 times larger than that of ZX50. The effect of grain size on yield strength can be obtained by Hall-Petch relationship as⁴¹:

$$\sigma_{GB} = \sigma_0 + k_y d^{-\frac{1}{2}} \quad (\text{Equation 1})$$

where d is the grain size, σ_0 is friction stress and k_y is HP-relation slope which are texture and grain size dependent. For the basal-textured Mg-Zn-Ca alloy, the experiential k_y is 228.51 $\text{MPamm}^{0.5}$ ⁴⁶. Calculated by the Hall-Petch equation, the decrement of YS for 1%, 2%, and 3% UGFs/ZX50 compared to ZX50 alloy are 180.7 MPa, 168.3 MPa, and 156.1 MPa, respectively. Hence, it can be concluded that the coarser grain is the main reason of the lower strength UGFs/ZX50.

Moreover, it also should be noticed that yield strength (YS) is impressively increased with the increasing UGFs content. For 1% UGFs/ZX50, the YS and ultimate tensile strength (UTS) are ~ 335.8 MPa and ~ 372.5 MPa respectively. With the UGFs content increase to 2%, the YS and UTS are both increased about 23 MPa, whereas the elongation is kept at the same level. The addition of 3% UGFs further improves the YS and UTS to maximum values as ~ 389.7 MPa and ~ 415.1 MPa without loss of ductility. Considering the similar grain size and other microstructure characteristics of UGFs/ZX50 composites (shown in Figure 3), it can be deduced that the enhanced strength mainly comes from the direct reinforcement of UGFs.

Another gripping information is that the elongation of UGFs/ZX50 has considerably enhanced, which is almost twice that of ZX50 alloy. This is mainly attributed to the graphite-Mg interface and the larger grain size which contributed to a stronger strain hardening behavior, inhibited the delocalized plastic strain, and resulted in better elongation of UGFs/ZX50 composites.⁵⁸

Figure 6B shows the thermal conductive properties of UGFs/ZX50 and ZX50. The measured physical parameters, including density ρ , specific heat C_p , thermal diffusivity α and thermal conductivity K , are listed in Table 1. As it shows, the thermal conductivity is efficiently enhanced by the introduction of UGFs. The thermal conductivity of ZX50 is ~ 123.1 $\text{W}/(\text{m}\cdot\text{K})$. The 1% UGFs/ZX50 have a thermal conductivity value of ~ 130.88 $\text{W}/(\text{m}\cdot\text{K})$, 2% UGFs/ZX50 reaches ~ 144.23 $\text{W}/(\text{m}\cdot\text{K})$, and 3% UGFs/ZX50 with ~ 138.16 $\text{W}/(\text{m}\cdot\text{K})$. The delightful enhancement degree is quite high compared with other Mg composites containing graphene or multi-walled carbon nanotubes.^{47,48}

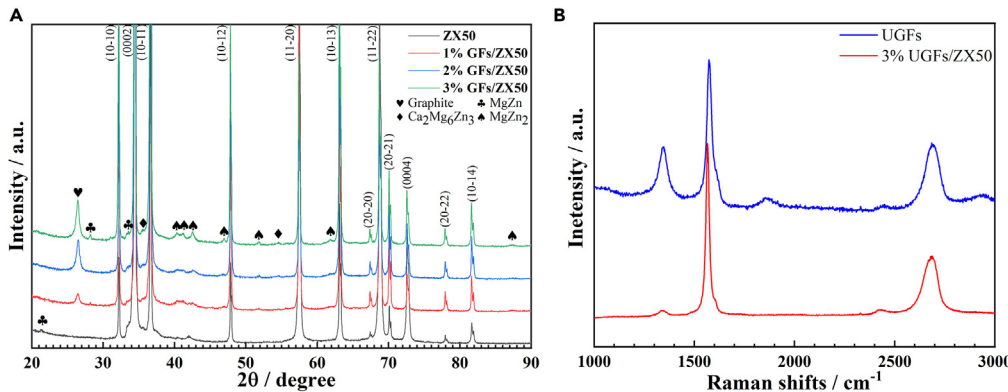


Figure 5. X-ray diffraction and Raman spectra analysis of as-extruded UGFs/ZX50 composite

(A) XRD patterns of the as-extruded ZX50 alloy and the UGFs/ZX50 composites.
(B) Raman spectra of raw UGFs and as-extruded 3% UGFs/ZX50 composite.

The yield strength and thermal conductivity of typical Mg alloys and composites are compared, as shown in Figure 6C.^{3,47–57} The dashed line depicts the mutually exclusive relationship of strength and thermal conductivity as commonly consented.^{1,3} In other words, the high thermal conductivity is harder to achieve for the high strength Mg alloys. The electrons are the main heat carriers in Mg, whereas any lattice imperfections will cause electron scattering, cut down the mean free path of electrons, causing the decrease of thermal conductivity.^{9,10} For instance, 1 atomic percent of Zn addition causes a reduction of thermal conductivity about 26.3 W/(m·K).³⁹ Therefore, the thermal conductivity of pure Mg (~156 W/(m·K)) is considered as a ceiling which hardly to be broken through. Traditional approaches to enhance Mg alloy strength mainly rely on the alloying element adding to achieve grain refining and dislocation introducing, which invariably cause the sacrifice of thermal conductivity to some extent. This trade-off dilemma not only just occurs in Mg alloy, but also extends to the Mg composites. Previous studies on carbon nanotubes/graphene reinforced Mg composites also demonstrate poor thermal conductivity improvements of ~5.2% and ~3.6%, respectively.^{47,48} In contrast, the UGFs/ZX50 shows a splendid thermal conductive strengthening of ~21 W/(m·K) (~17.1%). The excellent thermal conductivity and mechanical properties of UGFs/Mg-Zn-Ca composites can be ascribed to the following three factors: (1) The proper size of UGFs that ensures the optimal balance between the dispersion and content of UGFs; (2) the highly oriented UGFs⁵⁹; (3) the interface modification.^{36,44}

Interfacial structure

The interface layer observation and identification

Figure 7A shows the typical microstructure of as-extruded UGFs/ZX50 composites. The brightfield transmission electron microscopy (TEM) image shows the fine DRXed grain structure. The nano-precipitates were identified as MgZn₂ by SAED pattern. The graphite flakes marked by blue arrows show a parallel orientation. Moreover, the micrograph of disk-like UGFs indicates it had not been severely wrinkled during extrusion.

Figure 7B presents the high-resolution transmission electron microscopy (HRTEM) image of the interface. It shows a crystalline interface layer with super-nano scale thickness uniformly covering the graphite flake. The HRTEM micrograph in Figure 8A also shows the crystalline interface layer sandwiched by the graphite and Mg matrix, which is marked by the purple dotted lines. Graphite was determined by its characteristic layer structure and interlayer spacing (~0.35 nm), and the Mg matrix was identified by the HRTEM images and fast Fourier transform (FFT) patterns.

The crystalline interface layer was confirmed as CaCO₃ (Aragonite, Orthorhombic pnma 62) by the crystallography characteristic identification assisted by HAADF and EDS elements analysis (Figure 4). In Figure 7D, the characteristic interlayer spacing and the angle of (201) and (111) were identified as ~2.7 Å, ~3.4 Å and ~45.8°, respectively. These results agree with the aragonite with orthorhombic structure. The corresponding FFT pattern shown in Figure 7D confirms the characteristic plane of (201)_{CaCO₃}, (111)_{CaCO₃}, (110)_{CaCO₃}. The HRTEM analysis in Figure 8 demonstrates the CaCO₃ interface layer too. The atom scale observation and corresponding FFT analysis in Figures 8B and 8E confirm the characteristic interlayer spacing and the

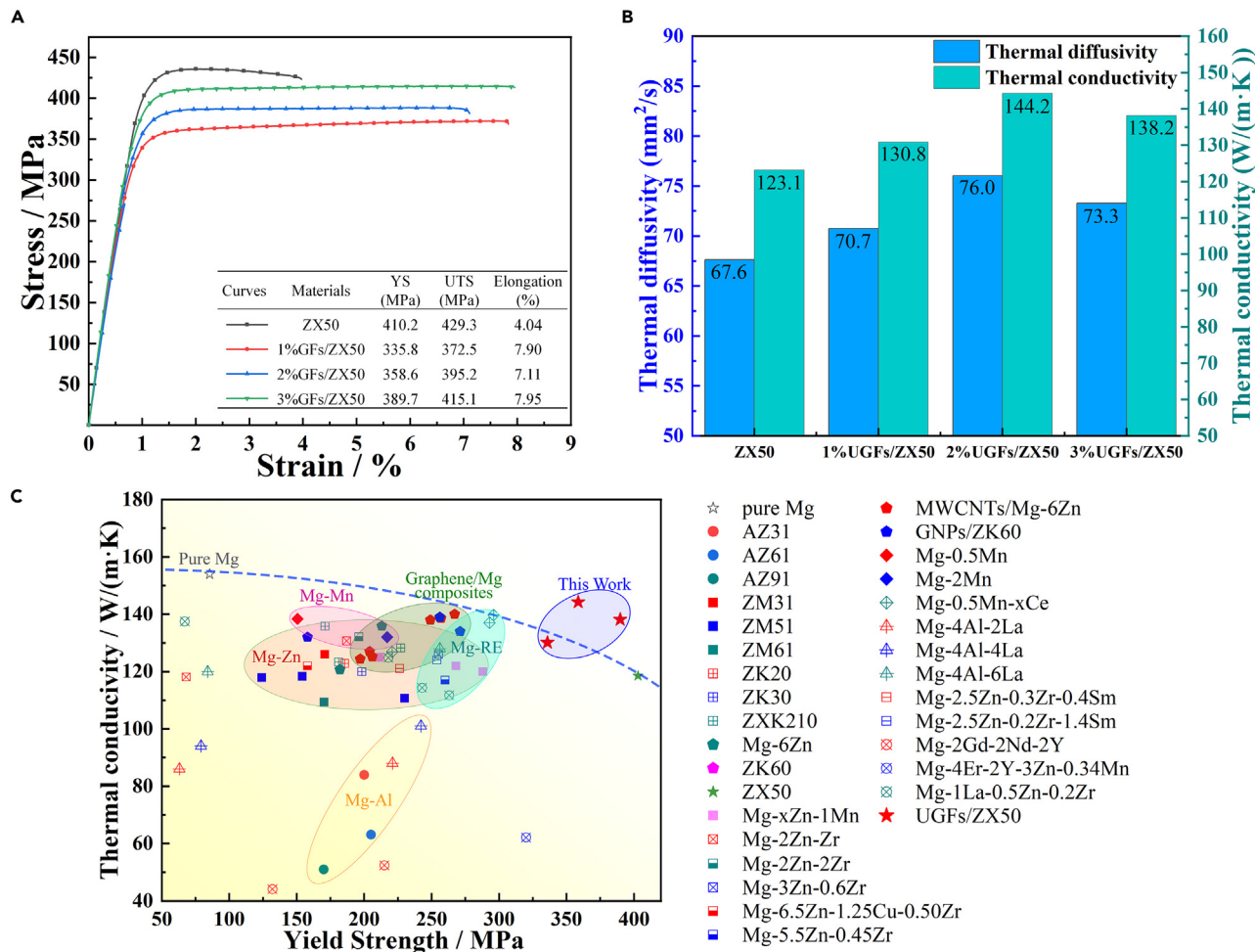


Figure 6. Mechanical and thermal conductive properties of the composites

(A) Tensile strain-stress curves.

(B) Thermal diffusivity and thermal conductivity properties.

(C) Relations of yield strength and thermal conductivity of UGFs/ZX50 and previously reported Mg matrix materials.^{3,47–57}

angle of crystallographic planes of CaCO_3 . The interlayer spacing and the angle of $(020)_{\text{CaCO}_3}$ and $(210)_{\text{CaCO}_3}$ and have been identified as $\sim 2.49 \text{ \AA}$, $\sim 2.52 \text{ \AA}$ and $\sim 60^\circ$ respectively, which are close to the theoretical values (JCPDS card NO. 96-901-5852). The presentation of CaCO_3 can also be verified by indexing the FFT pattern shown in Figure 8E. It is worth noting that the interface is very clean without occurring of pore, oxide, or amorphous substance. Moreover, the low-angle grain boundaries (LAGBs) with a junction to CaCO_3 layer can be observed, which may be induced by the hetero-interface for alleviating lattice strain.

The characteristics of Mg-aragonite interface

The HRTEM image in Figure 7D shows a zigzag Mg-aragonite interface at molecular scale. Moreover, it shows a kind of coherent interface Mg- CaCO_3 . The orientation relationship at the interface can be described as: $(201)_{\text{CaCO}_3} // (10 - 10)_{\text{Mg}}$, $[11 - 2]_{\text{CaCO}_3} // [0100]_{\text{Mg}}$. The d-value mismatch between (201) plane of CaCO_3 and the $(10-10)$ plane of Mg can be generated as follows:

$$\delta = \frac{d_{(10-10)_{\text{Mg}}} - d_{(201)_{\text{CaCO}_3}}}{d_{(10-10)_{\text{Mg}}}} \times 100\% = \frac{0.278 - 0.274}{0.278} = 1.44\% \quad (\text{Equation 2})$$

Likewise, another epitaxial relationship of $(-210)_{\text{CaCO}_3} // (0002)_{\text{Mg}}$ and $(020)_{\text{CaCO}_3} // (10 - 11)_{\text{Mg}}$ was revealed, as shown in Figure 8B. The FFT pattern of Figure 8B shown in Figure 8C further demonstrates

Table 1. Tested parameters of the thermal conductive properties

Materials	Density (g/cm ³)	Thermal diffusivity (mm ² /s)	Specific Heat Capacity (J/(g·K))	Thermal conductivity (W/(m·K))
ZX50	1.785 ± 0.008	67.634 ± 0.027	1.020 ± 0.0306	123.14 ± 4.298
1% UGFs/ZX50	1.807 ± 0.010	70.801 ± 0.058	1.023 ± 0.0307	130.88 ± 4.759
2% UGFs/ZX50	1.815 ± 0.007	76.045 ± 0.041	1.045 ± 0.0314	144.23 ± 4.968
3% UGFs/ZX50	1.827 ± 0.002	73.279 ± 0.050	1.032 ± 0.0310	138.16 ± 4.435

the crystallographic orientation and their relationships between Mg matrix and CaCO₃. The almost coincide dots demonstrate the epitaxial coherent orientation relationship.

The d-value mismatches were calculated as:

$$(-210)_{\text{CaCO}_3} // (0002)_{\text{Mg}}, [001]_{\text{CaCO}_3} // [0 - 110]_{\text{Mg}} : \delta = \frac{d_{(0002)_{\text{Mg}}} - d_{(-210)_{\text{CaCO}_3}}}{d_{(0002)_{\text{Mg}}}} \times 100\% = \frac{0.2605 - 0.2516}{0.2605} = 3.42\% \quad (\text{Equation 3})$$

$$(020)_{\text{CaCO}_3} // (10 - 11)_{\text{Mg}}, [001]_{\text{CaCO}_3} // [0 - 110]_{\text{Mg}} : \delta = \frac{d_{(10 - 11)_{\text{Mg}}} - d_{(020)_{\text{CaCO}_3}}}{d_{(10 - 11)_{\text{Mg}}}} \times 100\% = \frac{0.2452 - 0.2488}{0.2452} = 1.47\% \quad (\text{Equation 4})$$

The angle of the (-210)_{CaCO₃} and (020)_{CaCO₃} plane is 59.62°, whereas the angle of (0002)_{Mg} and (10 - 11)_{Mg} plane is 61.93°, so that the angle mismatch of these two is 2.31°.

$$(210)_{\text{CaCO}_3} // (10 - 1 - 1)_{\text{Mg}}, [001]_{\text{CaCO}_3} // [0 - 110]_{\text{Mg}} : \delta = \frac{d_{(10 - 1 - 1)_{\text{Mg}}} - d_{(210)_{\text{CaCO}_3}}}{d_{(10 - 1 - 1)_{\text{Mg}}}} \times 100\% = \frac{0.2452 - 0.2516}{0.2452} = 2.61\% \quad (\text{Equation 5})$$

The angle of the (-210)_{CaCO₃} and (210)_{CaCO₃} plane is 60.76°, whereas the angle of the (10 - 11)_{Mg} and (0002)_{Mg} plane is 61.93°. Thus, the angle mismatch of these two is 1.17°.

Figures 8G–8I show the inverse Fourierfiltered (IFFT) images of the yellow box a-3 in **Figure 8A** under the axis of [0002]_{Mg}, [10-10]_{Mg} and [10-11]_{Mg}. The severe lattice distortion in **Figure 8I** indicates the mismatch at the direction of [10-10]_{Mg}. On the other hand, the good match under the axis of [0002]_{Mg} and [10-11]_{Mg} demonstrate the coherent relationship of Mg-CaCO₃ interface. Based on the analysis above, schematic diagram of the preferential orientation relationship between the CaCO₃ and Mg is illustrated in **Figure 8D**. It shows that some atom positions of the CaCO₃ and Mg crystal lattice almost coincide with each other. Besides, the orientation and the coherent relationships have also been demonstrated briefly.

The characteristics of graphite-CaCO₃ interface

The bonding behavior of graphite-CaCO₃ interface was analyzed by XPS (X-ray photoelectron spectroscopy). The XPS C1s and O1s spectrum of 3% UGFs/ZX50 composite are shown in **Figures 9A** and **9B**, respectively. The binding energies at 290.2 eV and 532.0 eV corresponded to the C and O bonding of [CO₃]²⁻ anion,⁶⁰ and carbon bonds of graphite with the sp² and sp³ hybridization were also detected at binding energies of 284.5 eV and 285.6 eV. A small amount of C=O and C-O bonds at 284.5 eV and 285.6 eV may come from the heteroatom substitutional defects or other organic contaminants. The binding energy of 529.6 eV indicates the existence of metal oxides,⁶⁰ which can be from the oxidation of Mg during the sample preparation.

More excitingly, the metal-carbon ionic bond was detected at binding energy of 282.0 eV, which was originated from the graphite-Ca interaction at the interface.^{17,60,61} The carbon (C) atoms are held together by strong covalent bonds in the basal graphitic plane. The remaining p_z-orbital of carbons allows them to interact with metals. The strength of Metal-Carbon interaction depends on the extent of the electron cloud overlap, which is reflected in the equilibrium atomic distances D_{eq} and adsorption energies E_{ads} value.^{17,62} It was reported that the Mg-carbon surface separation distance is ~3.3 Å, which is close to the distance of the van der Waals gap in graphite (3.4 Å).⁶² Thus, graphite interplays with the Mg matrix only by

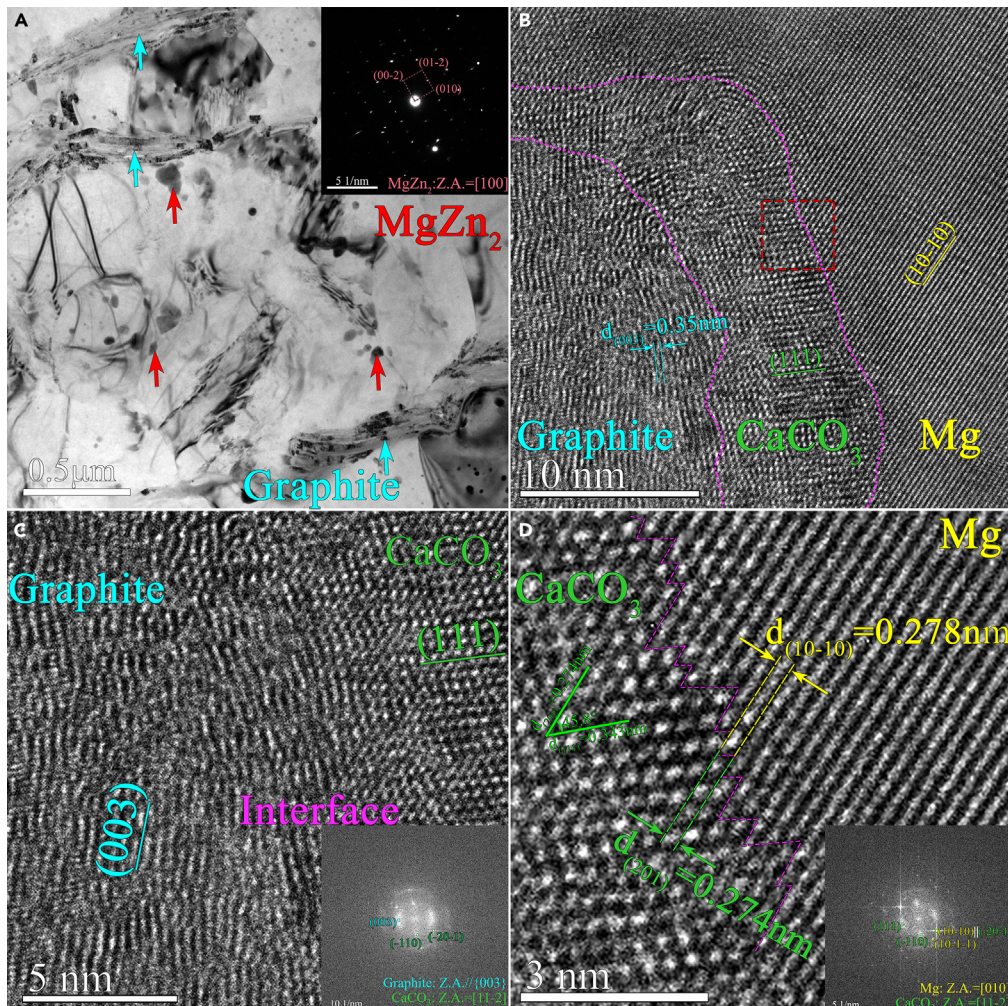


Figure 7. TEM microstructure and interfacial structure examination

- (A) TEM bright field image of UGFs and Mg matrix in its vicinity.
- (B) HRTEM of graphite-Mg interface.
- (C) Graphite-aragonite interface and its corresponding fast Fourier transform (FFT) patterns.
- (D) Aragonite-Mg interface and its corresponding FFT pattern.

micromechanical interlocking, leading to very weak interfacial adhesion. The Zn atoms also demonstrate a weak physisorption with graphite as D_{eq} value is about 3.27 Å⁶²

The Ca atoms, on the other hand, perform much stronger interaction with graphite. The HRTEM image of the interface and the measured plane spacing shown in Figures 9C and 9E indicates that carbon atoms at the graphite surface shows an interatomic spacing of 2.84 Å with the Ca atoms of CaCO₃. The small atomic distance indicates a strong orbital overlapping of Ca with C, a kind of strong chemisorbed interaction. Such results are in line with the density functional theory (DFT) simulations.⁶² It is believed that the Ca atom readily donates one of its s-electrons to the nearest neighbor carbon atom in the graphite.^{62,63} The charge transfer from the Ca to the neighboring carbon would produce a strong ionic bond, with the distance between the carbon and Ca atoms of ~2.3 Å.⁶² Hence, the XPS spectra at 282.0 eV of C1s in Figure 9A, indicating the strong C-metal bond, can be confirmed as C-Ca ionic bond.

Thermodynamics and kinetics analysis of the interfacial reaction

The crystalline aragonite layer sandwiched by the graphite and Mg matrix was originated from the *in situ* interfacial reaction. Hence, the corresponding thermodynamics and kinetics analysis were conducted for an in-depth understanding of the formation mechanism of the intermediate layer.

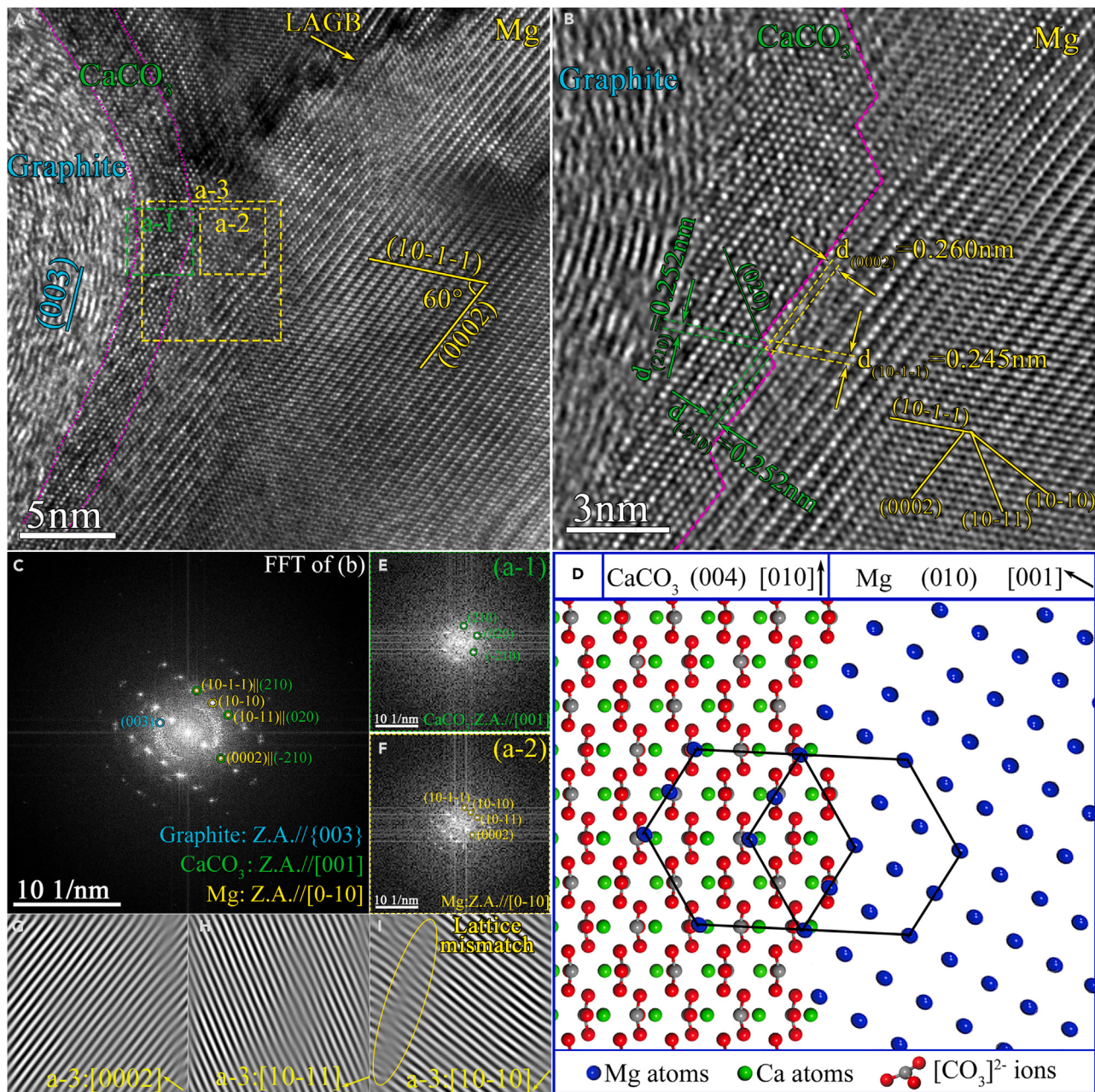


Figure 8. Interfacial structure characterization

(A and B) HRTEM of the Graphite-Mg interface.

(C) FFT pattern of figure (B).

(D) Schematic diagram of the preferential orientation relationship between CaCO_3 and Mg.

(E) FFT pattern of the green box a-1(CaCO_3 layer) in figure (A); (F) FFT pattern of the yellow box a-2 (Mg matrix) in figure (A).

(G and H) Inverse Fourierfiltered (IFFT) images of the yellow box a-3 showing a coherent orientation relationship of $(0002)_{\text{Mg}}//(-210)_{\text{CaCO}_3}$ and $(10-11)_{\text{Mg}}//(020)_{\text{CaCO}_3}$.

(I) IFFT images of the yellow box a-3, the lattice distortion indicates a mismatch of $[10-10]_{\text{Mg}}$ and CaCO_3 .

Reaction thermodynamics

As the UGFs were added in Mg alloy melt, the Ca solute atoms in the melt were absorbed onto the graphite surface, and met the carbon and oxygen atoms, then the spontaneous reaction happened. The oxygen may

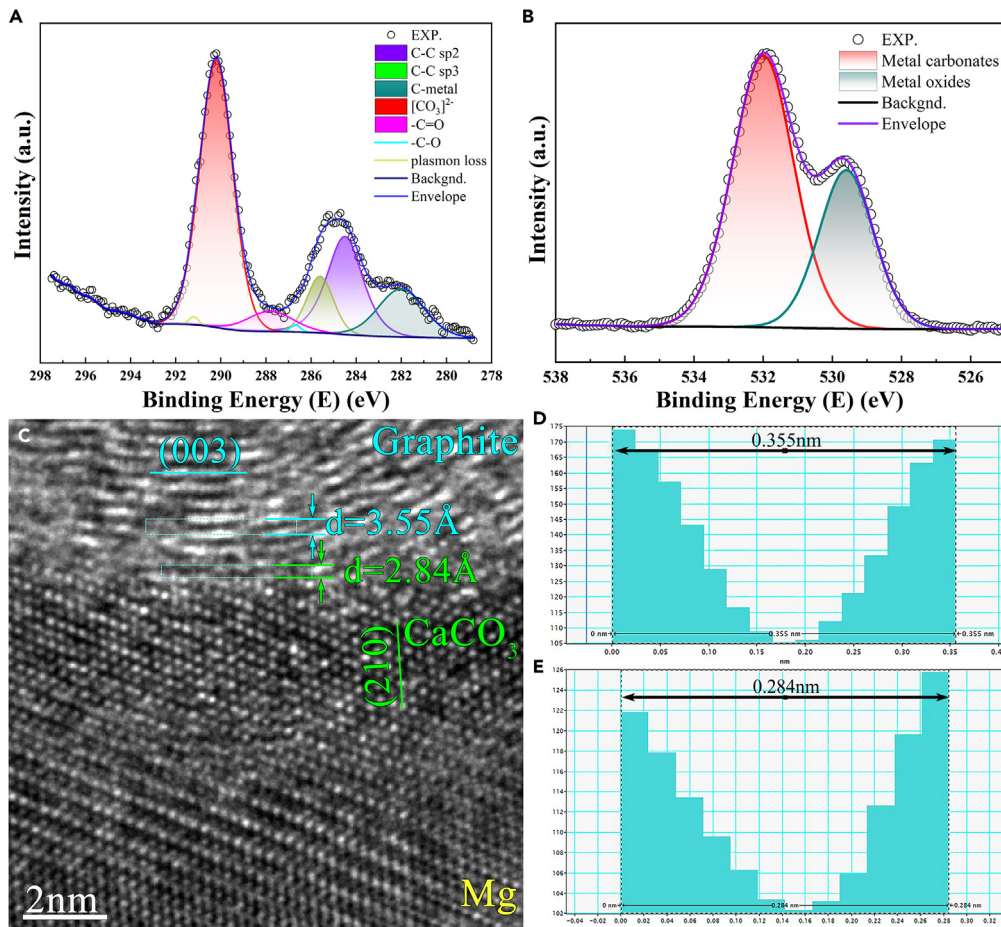
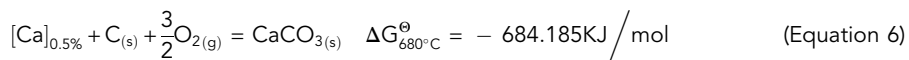


Figure 9. Interfacial features between graphite and CaCO_3

(A and B) C1s and (b) O1s XPS spectra for the 3% UGFs/ZX50 composite.
(C) HRTEM of the interface.
(D) Measured distance of basal graphitic plane.
(E) Measured distance of atoms at the interface.

come from adsorbed oxygen molecules or oxygenic groups on the graphite surface. The interfacial reaction can be expressed as:



where $[\text{Ca}]_{0.5\%}$ represents the Ca dissolved in the metallurgical solution. Standard Gibbs free energies of the reaction can be drawn by

$$\Delta_r G^{\theta} = \Delta_f G_{\text{CaCO}_3}^{\theta} - \Delta_{\text{sol}} G_{[\text{Ca}] 0.5\%}^{\theta} - \Delta_f G_{\text{C}}^{\theta} - \frac{3}{2} \Delta_f G_{\text{O}_2}^{\theta} \quad (\text{Equation 7})$$

where $\Delta_{\text{sol}} G_{[\text{Ca}] 0.5\%}^{\theta}$ is dissolution Gibbs energy of $[\text{Ca}]_{0.5\%}$, represents the partial molar excess Gibbs free energy of mixing the solute component Ca into solvent Mg, can be obtained from $\Delta_{\text{sol}} G_{[\text{Ca}] 0.5\%}^{\theta} = \mu_{\text{Ca}}^{\theta} - \mu_{\text{Ca}}^{*}$.⁶⁴ The μ_{Ca}^{θ} and μ_{Ca}^{*} represent the chemical potential of Ca in the metallurgical solution and the chemical potential of pure Ca, which was calculated with Thermal-Calc software. $\Delta_f G_{\text{CaCO}_3}^{\theta}$, $\Delta_f G_{\text{C}}^{\theta}$, and $\Delta_f G_{\text{O}_2}^{\theta}$ are the standard free energy of formation of CaCO_3 , C and O_2 respectively, which were deduced by the formula as $\Delta G_T^{\theta} = \Delta H_T^{\theta} - T\Delta S_T^{\theta}$. The thermodynamic parameters of the substances can be found from thermochemical properties databook.⁶⁵ Figure 10A shows the standard Gibbs-free energies ΔG_T^{θ} of oxidation and carbonation of Ca. The ΔG_T^{θ} is decreased with the decrease in the temperature, indicating that the spontaneous chemical changes become easier at lower temperature. Actually, the value of ΔG_T^{θ} alone is

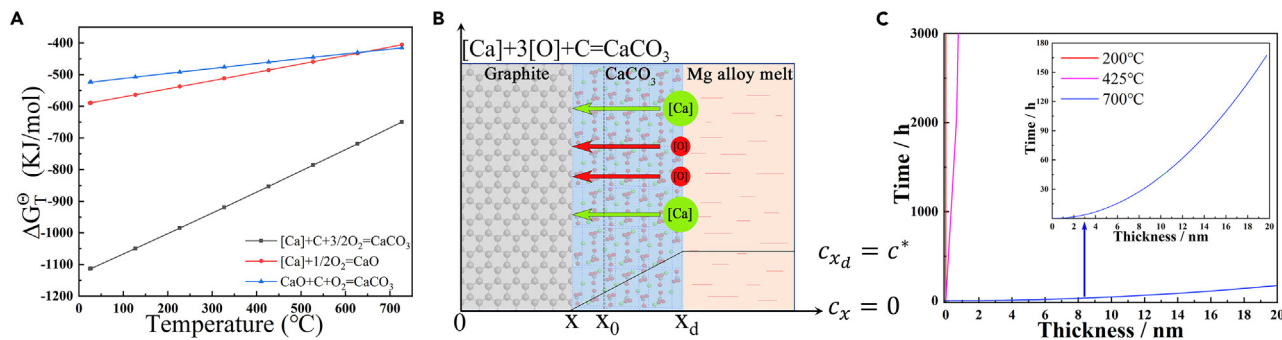


Figure 10. Thermodynamics and kinetics analysis of the interfacial reaction

- (A) Plot of standard Gibbs free energies versus temperature.
 (B) Illustration of the diffusion processes which controlled the reaction.
 (C) Plot of the thickness of CaCO₃ layer versus time.

insufficient to reflect the difficulty and degree of the interfacial reaction, as it is a multi-phase reaction involved with mass transfer, atom diffusion, breaking and forming of chemical bonds, nucleation and growth of newly formed phases.

Reaction kinetics

Once the interfacial reaction occurs, the reactants (graphite and Ca) were partitioned by the product layer (CaCO₃), as shown in Figures 7B and 8A. The graphite surface is readily covered by the newly formed crystalline CaCO₃ layer, because CaCO₃ has higher molar volume (35.1 cm³/mol) than graphite (5.6 cm³/mol).⁶⁶ Hence, the proceeding of the reaction mostly relies on the diffusion of reactants across the interface. The CaCO₃ product layer became thicker as the reaction progress. The relationship between the reaction time and the thickness of CaCO₃ layer can be obtained by solving the Equation S11 in supplemental information, which can be expressed as:

$$\frac{M_C}{\rho_C} \cdot D \cdot C^* \cdot t = \frac{1}{2}(Z - 1) \cdot x^2 - (Z - 1)x_0 \cdot x + \frac{1}{2}(Z - 1)x_0^2 \quad (\text{Equation 8})$$

where ρ_C is the density of graphite, M_C is the molar mass of the graphite, D is the diffusion coefficient (cm²/s), C^* is the concentration of reactant at Mg-CaCO₃ interface (as depicted in Figure 10B), t is time, x_0-x is the consumed graphite thickness, and x_d-x is the thickness of CaCO₃ layer, Z is 6.583 for this interfacial reaction. The detailed deduction of interfacial reaction kinetics is described in Supplemental Text S1. The self-diffusion coefficient of calcium carbonate can be obtained from the ref.⁶⁷

Plots of the thickness of CaCO₃ product layer versus time and temperature are presented in Figure 10C. The varied thickness of CaCO₃ layer versus time is analogous to the classic parabola rate law model,⁶⁸ which demonstrates that the growth rate of CaCO₃ production layer becomes more and more difficult with time going on. The thickness of CaCO₃ layer also relates to the temperature, as it exerts significant influence on the diffusion which can be described by the Arrhenius theory⁶⁷:

$$D_L = D_0 \exp(-E_q/RT) \quad (\text{Equation 9})$$

where D_0 is the pre-exponential factor and E_q the activation energy.

As calculated in Figure 10C, it can be deduced that the CaCO₃ layer was formed and grew to a thickness of 3–8 nm during stir-casting (~700°C) and subsequent homogenizing (~430°C). The amorphous carbon (in view of the graphitization degree of UGFs) with more active chemical character and free diffusion ability, may lead to a slightly plus deviation on the thickness of CaCO₃ layer. At temperature lower than 200°C, the diffusion almost stopped, as the diffusion coefficient decreases to 6.37×10^{-24} cm²/s, which is 7 orders of magnitude lower than that at 700°C. In ionic crystals, the diffusion predominantly taking place at crystal defects, and should always meet the electroneutrality condition for ionic diffusion. Hence, the aragonite is very stable in the nature.⁶⁷ The difference in thickness of CaCO₃ layer shown in Figures 7B and 8B may partially result from the different diffusion rate and growth rate along different crystallographic direction.

Effects of the *insitu* reaction on the graphite-Mg interface

Ameliorated interfacial compatibility

Interfacial compatibility affected by the interfacial energy which is related to the wettability and bonding behavior of hetero-interface. Wettability refers to the ability of Mg melt to spread on graphite surface, affecting the interface quality and UGFs distribution.³⁶ The successful incorporation of UGFs into Mg needs the melt to fully wet the graphite. It is reported that the poor wettability between graphite and most metals can usually cause nano-sized voids at graphite/metal interfaces.⁴⁴ In addition, the interactions between the solidifying interfaces and the graphite flakes, which determine the UGFs distribution in casting ingot, are also intensively affected by the wettability.³⁶ It is generally believed that the poor wettability of graphite flakes increases its tendency to agglomerate.³⁶

The wettability of a solid by a liquid is indicated by the "contact angle" θ , which can be expressed by Equation 10 under the status of equilibrium.⁶⁹

$$\theta = \arccos\left(\frac{\gamma_{GS} - \gamma_{LS}}{\gamma_{GL}}\right) \quad (\text{Equation 10})$$

where γ_{GS} , γ_{GL} , γ_{LS} are interface energy of the gas-solid, gas-liquid and liquid-solid, respectively. The θ value decrease with the increase of $\left(\frac{\gamma_{GS} - \gamma_{LS}}{\gamma_{GL}}\right)$. When the value of $\left(\frac{\gamma_{GS} - \gamma_{LS}}{\gamma_{GL}}\right)$ is less than 0, the "contact angle" is bigger than 90°, the wettability is bad. Considering the surface energy of Mg melt is a constant ($\gamma_{GL} = 0.56 \text{ J/m}^2$),⁶⁹ it can be concluded that the "contact angle" θ depends on the $(\gamma_{GS} - \gamma_{LS})$ value. If the surface energy of solid can be increased and/or the interface energy of solid-liquid can be decreased, the $\left(\frac{\gamma_{GS} - \gamma_{LS}}{\gamma_{GL}}\right)$ value would increase which further results in a lower contact angle implying an improved wettability.⁷⁰

Generally, the interface reaction decreases the interface energy of graphite-Mg interface. From the perspective of interface interaction, the origin of the poor wettability is the weak physical adsorption, which is governed by van der Waals type interactions. As a rule, however, the work of adhesion can be largely increased when chemical interactions occur.⁶⁹ The preferential orientation between crystalline CaCO₃ and Mg were readily formed during the fabrication process, driven by the local interfacial energy minimum. Strictly speaking, the interfacial energy between two crystalline materials comprises chemical and structural components. Anion-cation bond of ionic crystals has significantly lower binding energy than anion-anion or cation-cation bond, in metals and intermetallic compounds.⁷¹ The [CO₃]²⁻ anion at the CaCO₃ surface may afford low energy site for the adsorption of Mg atom.

Besides, the structural component, which arises from the atomic site misfit across the interface, also contributes to the interfacial energy. As depicted above, the Mg-aragonite interface shows several coherent relationships where interplanar spacing mismatch are only ~1.44% for (201)_{CaCO₃}//(10-10)_{Mg}, and ~1.47% for (020)_{CaCO₃}//(10-11)_{Mg}. The small interatomic spacing misfit usually contributes to low elastic strain energy of the interface, leading to the low interfacial energy of the preferential orientation and coherent interfacial structure.⁷¹ It is well acknowledged that interphase boundary energies of coherent interfaces are the lowest (5–200 mJ/m²), followed by those of semi-coherent (200–800 mJ/m²) and incoherent interfaces (800–2500 mJ/m²).⁷²

On the other hand, the surface energy of graphite is only 0.165 J/m², whereas the surface energy of aragonite is 1 J/m².^{73,74} This indicates the formation of aragonite layer increase the surface energy of the reinforcements. Hence, it can be concluded that the interface reaction increases the surface energy of solid and decrease the interface energy of solid-liquid simultaneously, which result in an improved wettability.

The UGFs/ZX50 composites show a good dispersion of UGFs in Mg matrix. The observation on interfacial structure (Figures 7B and 8B) further confirms the CaCO₃ layer is clean and uniformly covered the graphite. These phenomena demonstrate a good wettability and interfacial compatibility which was ameliorated by the interfacial reaction. Significantly, the lower interfacial energy usually makes the interface stable and strong.^{17,75}

Strengthened interface bonding

The graphite has a layer structure with a theoretical layer spacing of 3.35 Å. And each carbon atom within a layer is bonded to three neighbors at distance of 1.42 Å. The bonds in the basal graphitic plane are strong, thus it conferred strong mechanical and thermal conductive properties to graphite along basal plane. A recently *in situ* tensile study¹⁶ on multilayer graphene identified that the 50 nm thickness graphite performs

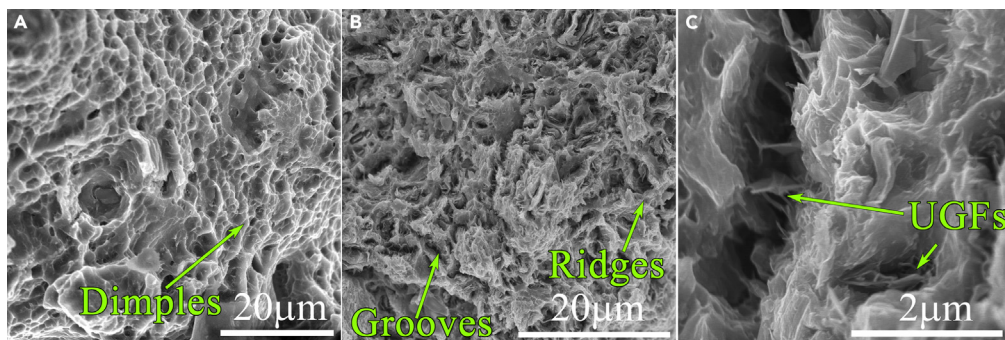


Figure 11. Scanning electron microscope images showing the fracture features

(A) Fracture morphology of ZX50 alloy; (B and C) Fracture morphology of 3% UGFs/ZX50 composite.

an excellent in-plane fracture strength as high as ~1.06 GPa. As expected, the highly graphitized and highly oriented graphite shows very high in-plane thermal conductivity up to 1950 W/(m·K).¹⁵ Hence, the strong interface bonding is of vital importance for adequately utilizing the advantages of graphite.

Aragonite, one polymorph of CaCO₃, is the main composition of mollusk shell in the natural world which is famous for its toughness. It was reported that the Young's modulus, ultimate tensile strength, and elongation to fracture of aragonite are ~142 GPa, ~5 GPa, and ~5%, respectively.⁷⁶ Therefore, it can be deduced that the excellent mechanical properties of the CaCO₃ layer can assure the strengthening efficacy of UGFs.

As analyzed above, there are Ca-C ionic bonds produced at the graphite-CaCO₃ interface. On the other side, the preferential coherent Mg-CaCO₃ interface also offers a strengthening effect. During the deformation, lattice defects (e.g., point defects and dislocations) tend to thermo-mechanically recover at boundaries. Study on graphene/metal composites demonstrates that the weak graphene-metal interfacial bonding limits the strengthening effect because of the interface-mediated plasticity takes place and the reduction of load carrying capability.⁷⁷ Comparatively, the coherent hetero-interface of UGFs/ZX50 composites with low interface energy affords higher thermomechanical stability, which is able to inhibit dislocation annihilations and restrain the deformation behavior.⁷⁵ Therefore, it can be deduced the interface reaction decreases the interface energy of graphite-Mg, and further makes the interface stable and strong.^{17,75}

The YS of 1%, 2% and 3% UGFs/ZX50 are ~335.8 MPa, ~358.6 and ~389.7 MPa, respectively. The impressive improvement (~54 MPa) can be ascribed to the strengthening behavior of UGFs. It is reported that effective load transfer strengthening can be obtained by reinforcements with large aspect ratio aligning along the tensile direction.^{18,78,79} The representative morphologies taken from the tensile fracture surfaces of 3%UGFs/ZX50 composite shown in Figures 11B and 11C verified the load transfer phenomenon. The fracture surface of UGFs/ZX50 composite (Figure 11B) exhibits many sharp grooves and ridges, which is different from typical fine-grain Mg alloy (Figure 11A). The special characteristic of fracture surface indicates that the propagation of microcracks was deflected and hindered by the highly oriented UGFs alliance. A large amount of UGFs was sticking out of the fracture matrix in the bottom of dimples and on the surface of blade type edges. The wrinkled and straight UGFs show a highly paralleled orientation along the tensile direction (Figure 11C). During the tensile deformation, the load transfer originated from the deformation incompatibility leads to higher stress at the interface and UGFs. The high in-plane strength of UGFs is adequate to ensure it cannot be fractured easily. In addition, the coherent hetero-interface applied strong restraint effect on the deformation behavior of Mg matrix, benefiting to the load transfer as a result.

Via the shear-lag model, the strength improvement from load transfer of UGFs can be evaluated. A probability theory, developed by Fukuda and Chou, to examine the effects of load transfer on the strength of composites can be expressed as⁷⁸:

$$\Delta\sigma_{LT} = \frac{1}{2}\sigma_m f_v \frac{D}{T_k} C_0 \quad (\text{Equation 11})$$

where σ_m is the yield strength of matrix alloy, f_v is the volume fraction of UGFs, D is average diameter of UGFs (~2.0 μm), T_k is thickness of UGFs (~0.1 μm), and C_0 is the UGFs orientation factor (~0.89). Based on, Equation 11,

the value of σ_m can be calculated as ~ 303 MPa, which is close to the value estimated by strengthening contribution analysis model.^{41,80} The load transfer strengthening of the increment in yield strength for 1%, 2% and 3% UGFs were estimated as ~ 27.05 MPa, ~ 54.09 MPa, and ~ 81.14 MPa, respectively.

The significant load transfer strengthening behavior of UGFs depends on its strong bonding with Mg matrix. The mathematical relationship between load transfer strengthening efficiency (R_{LT}) and interface bonding strength τ can be expressed as¹⁸:

$$R_{LT} = \frac{\Delta\sigma_{LT}}{f_v\sigma_m} = \frac{\tau D}{2\sigma_m T_k} - 1 \quad (\text{Equation 12})$$

where σ_c is the strength of composites; σ_m is the Mg matrix strength of UGFs/ZX50 composites ($\sigma_m \approx 303$ MPa), f_v is the volume fraction of UGFs, D is average diameter of UGFs, T_k is thickness of UGFs. Based on Equation 12, the R_{LT} and τ values were estimated as ~ 8.93 and ~ 300.9 MPa, respectively. Hence, it can be concluded that the UGFs perform a good strengthening effect because of its relatively strong interface bonding, during the tensile deformation. Moreover, the good elongation of UGFs/ZX50 (as shown in Figure 6A) is also ascribed to the delayed failure caused by the highly oriented UGFs alliance.

Facilitated interfacial thermal conduction

The high purity graphite possesses an extremely high in-plane thermal conductivity about 2000 W/(m·K), owing to the large ballistic thermal conductance and long phonon mean free path (MFP).¹³ Although it shows a great potential in thermal management applications, the high thermal conductivity UGFs/ZX50 composites are not easily obtained. The highly paralleled distribution of graphite is vitally important as the strong thermal conductive anisotropy of graphite. Another crucial issue is the interfacial thermal resistance (ITR).⁸¹ ITR represents a barrier to the heat flow associated with the differences in the phonon spectra of the two phases and the possible weak contact at the interface.

Figure 12A shows the schematic of the thermal transport across the interface, which relies on whether the incident phonon is transmitted or not.⁸² For each introduced interface layer, one more new interface and thermal barrier zone will be added. Analogous to the concept of series of electrical resistance, the interfacial thermal resistance of Mg/CaCO₃/Graphite can be similarly expressed as⁸¹:

$$R = R_1 + R_2 + R_3 \quad (\text{Equation 13})$$

where the R represents the ITR as depicted in Figure 12A. The ITR of Mg/CaCO₃ and CaCO₃/Graphite interface can be estimated by the acoustic mismatch model (AMM). The reciprocal of ITR is the interfacial thermal conductance (ITC) h which can be obtained by⁸¹:

$$h \approx \frac{1}{4} \rho c v \eta = \frac{1}{2} \rho_m c_m \frac{v_m^3}{v_r^2} \frac{\rho_m v_m \rho_r v_r}{(\rho_m v_m + \rho_r v_r)^2} \quad (\text{Equation 14})$$

where ρ , c , v and η are mass density, specific heat capacity, sound velocity and average probability for the transmission of phonon across the interface, respectively. The ITR of CaCO₃ layer which relates to the thickness can be calculated by:

$$R_{\text{CaCO}_3} = \frac{T_{\text{CaCO}_3}}{K_{\text{CaCO}_3}} \quad (\text{Equation 15})$$

where T_{CaCO_3} and K_{CaCO_3} are the thickness and thermal conductivity of CaCO₃ layer ($K_{\text{CaCO}_3} \approx 2.5$ W/(m·K)).⁸³ The material parameters for the calculations were given in Table 2. Then, the interfacial thermal conductance values (reciprocal of ITR) can be calculated as shown in Figure 12B. It shows that the interfacial thermal conductance value becomes lower for a thicker CaCO₃ layer.

The calculated ITR value of Mg/graphite interface is 5.39×10^{-8} m²K/W, which is of the same order of magnitude for Al/graphite interface.⁵⁹ However, the calculated ITR of Mg/CaCO₃(10 nm)/graphite interface is 3.03×10^{-8} m²K/W, which is reduced about 43.8% compared to that of Mg/graphite. As depicted in Figure 12B, the red line indicates superior interfacial thermal conductance of Mg/CaCO₃/graphite compared to that of Mg/graphite interface, implying a better performance in thermal conductive property of UGFs/ZX50 composite by the *in situ* interfacial modifying. In other word, the interfacial thermal resistance is apparently reduced with the introduction of super-nano CaCO₃ layer. From a theoretical point of view, the scattering of phonons at the hetero-interface is mainly because of the existence of an interfacial thermal barrier from acoustic mismatch. Accordingly,

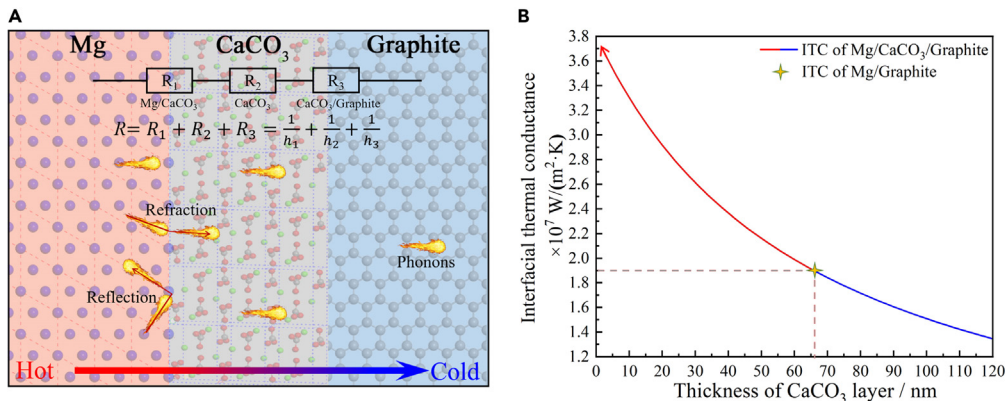


Figure 12. Interfacial thermal conductive behavior described by acoustic mismatch model

(A) Thermal transport schematic of the interface.

(B) Plot of the theoretical interfacial thermal conductance (ITC) with respect to the thickness of CaCO_3 layer.

the transmission of a phonon between two phases depends on the existence of common vibration frequencies for the two phases.⁸⁵ The CaCO_3 intermediate layer may play a role in healing the huge gap between Mg and graphite because of its decent specific heat and phonon velocity. This healing effect performs a higher coupling degree and finally alleviates the interface scattering and leads to a high transmission efficiency of the carriers.²⁴ During the heat transfer process, vibration harmonic mismatch, acoustic mismatch, and modulus mismatch of phonons are generated at the interfaces. Moreover, the strong interface bonding, good wettability, high purity, and few defects are also beneficial to the interfacial thermal conductance, which can be ameliorated by the interfacial reaction as well.

Conclusion

In this work, UGFs/ZX50 composites have been successfully fabricated by semi-solid stir casting assisted with ultrasonic vibration, a low cost and convenient manufacturing route. The outstanding mechanical and thermal conductive properties benefit from the modified chemical interface bonding, which is anticipated to help in providing new insights into carbon-metal interface modification. Specific conclusions can be drawn as follows: (1) The UGFs/ZX50 composites exhibit excellent mechanical and thermal conductive properties with the maximum YS of $\sim 389.7 \text{ MPa}$, elongation of $\sim 7.9\%$, and the maximum thermal conductivity of $\sim 144 \text{ W/(m}\cdot\text{K)}$. The excellent mechanical properties and thermal conductivity mainly ascribe to the interface modification. (2) A novel crystalline CaCO_3 interface layer with thickness of a few nanometers was identified in the Mg matrix composites for the first time. The interface layer is clean without defects such as pore, oxide, or other amorphous substance. The strong ionic bonding of graphite- CaCO_3 interface was revealed. On the other side, several preferential epitaxial relationships between Mg- CaCO_3 interface were demonstrated. (3) The interfacial reaction of $[\text{Ca}]_{0.5\%} + \text{C}_{(\text{s})} + 3[\text{O}] = \text{CaCO}_{3(\text{s})}$ happened at the graphite surface. The corresponding thermodynamics and kinetics analysis were conducted to help understand the formation mechanism. (4) The theoretical calculation indicates superior interfacial thermal conductivity of Mg/ CaCO_3 /graphite, implying the facilitated interfacial thermal conduction by the *in situ* interfacial modification.

Limitations of the study

Although the UGFs/ZX50 composites perform excellent mechanical and thermal conductivity synergy, the corresponding tensile deformation and thermal conductive behaviors affected by graphite-Mg interface are still hard to be elaborated clearly at the micro/atomic level because of the limitation of characterization technology. In the follow-up research, it is expected to develop new methods to help us understand the underlying mechanism more deeply. Moreover, architectural designs and controls of graphite flakes also need to be carried out in future work.

STAR★METHODS

Detailed methods are provided in the online version of this paper and include the following:

- KEY RESOURCES TABLE
- RESOURCE AVAILABILITY

Table 2. Material parameters for theoretical calculation^{59,82-84}

Material	Density (Kg/m ³)	Specific heat (J/(kg·K))	Phonon velocity (m/s)
Mg	1.80	980	3298
CaCO ₃	2.85	837	3480
Graphite	2.25	710	14800

- Lead contact
- Materials availability
- Data and code availability

● **EXPERIMENTAL MODEL AND SUBJECT DETAILS**

● **METHOD DETAILS**

- Material fabrication
- Microstructure analysis
- Thermal conductivity and mechanical property test

● **QUANTIFICATION AND STATISTICAL ANALYSIS**

SUPPLEMENTAL INFORMATION

Supplemental information can be found online at <https://doi.org/10.1016/j.isci.2023.106505>.

ACKNOWLEDGMENTS

This work was supported by the “National Natural Science Foundation of China” (Grants. 52271109 and 52001223). The authors also thank the Support from the Fundamental Reserch Program of Shanxi Province (Grant: 202103021223043), the “National Key Research and Development Program for Young Scientists” (Grant. 2021YFB3703300), and the Special Fund Project for Guiding Local Science and Technology Development by the Central Government (Grant. YDZJSX2021B019).

AUTHOR CONTRIBUTIONS

L.Z. fabricated the materials, conceived the idea, supervised the project, and wrote the manuscript. K-K.D., C.X., and K-B.N. provided facilities and guidance for material fabrications. C-J.W. and Q-X.S. performed part of the material characterizations. Y.L. provided help with fabrication of materials. J.W. provided help with material characterizations. All the authors revised and approved the manuscript.

DECLARATION OF INTERESTS

The authors declare that they have no known competing financial interests or personal relationships that could have appeared to influence the work reported in this paper.

INCLUSION AND DIVERSITY

We support inclusive, diverse, and equitable conduct of research.

Received: October 3, 2022

Revised: March 8, 2023

Accepted: March 23, 2023

Published: March 28, 2023

REFERENCES

1. Song, J., She, J., Chen, D., and Pan, F. (2020). Latest research advances on magnesium and magnesium alloys worldwide. *Journal of Magnesium and Alloys* 8, 1–41. <https://doi.org/10.1016/j.jma.2020.02.003>.
2. Yang, Y., Xiong, X., Chen, J., Peng, X., Chen, D., and Pan, F. (2021). Research advances in magnesium and magnesium alloys worldwide in 2020. *Journal of Magnesium and Alloys* 9, 705–747. <https://doi.org/10.1016/j.jma.2021.04.001>.
3. Li, S., Yang, X., Hou, J., and Du, W. (2020). A review on thermal conductivity of magnesium and its alloys. *Journal of Magnesium and Alloys* 8, 78–90. <https://doi.org/10.1016/j.jma.2019.08.002>.
4. Sørensen, S.S., Bødker, M.S., Johra, H., Youngman, R.E., Logunov, S.L., Bockowski, M., Rzoska, S.J., Mauro, J.C., and Smedskjaer, M.M. (2021). Thermal conductivity of densified borosilicate glasses. *J. Non-Cryst. Solids* 557, 120644. <https://doi.org/10.1016/j.jnoncrysol.2021.120644>.
5. Choy, C.L., Luk, W.H., and Chen, F.C. (1978). Thermal conductivity of highly oriented polyethylene. *Polymer* 19, 155–162. [https://doi.org/10.1016/0032-3861\(78\)90032-0](https://doi.org/10.1016/0032-3861(78)90032-0).

6. Ashworth, T., Johnson, L.R., Hsiung, C.Y., and Kreitman, M.M. (1973). Use of the linear heat flow for poor conductors and its application to the thermal conductivity of nylon. *Cryogenics* 13, 34–40. [https://doi.org/10.1016/0011-2275\(73\)90263-4](https://doi.org/10.1016/0011-2275(73)90263-4).
7. Suleiman, B.M., Larfeldt, J., Leckner, B., and Gustavsson, M. (1999). Thermal conductivity and diffusivity of wood. *Wood Sci. Technol.* 33, 465–473. <https://doi.org/10.1007/s00260050130>.
8. Yoon, Y.G., Car, R., Srolovitz, D.J., and Scandolo, S. (2004). Thermal conductivity of crystalline quartz from classical simulations. *Phys. Rev. B* 70, 012302. <https://doi.org/10.1103/PhysRevB.70.012302>.
9. Pan, H., Pan, F., Wang, X., Peng, J., Gou, J., She, J., and Tang, A. (2013). Correlation on the electrical and thermal conductivity for binary Mg-Al and Mg-Zn alloys. *Int. J. Thermophys.* 34, 1336–1346. <https://doi.org/10.1007/s10765-013-1490-3>.
10. Su, C., Li, D., Luo, A.A., Shi, R., and Zeng, X. (2019). Quantitative study of microstructure-dependent thermal conductivity in Mg-4Ce-xAl-0.5 Mn alloys. *Metall. and Mat. Trans. A* 50, 1970–1984. <https://doi.org/10.1007/s11661-019-05136-w>.
11. Wang, C.J., Deng, K.K., Nie, K.B., Shang, S.J., and Liang, W. (2016). Competition behavior of the strengthening effects in as-extruded AZ91 matrix: influence of pre-existed Mg₁₇Al₁₂ phase. *Mater. Sci. Eng., A* 656, 102–110. <https://doi.org/10.1016/j.msea.2016.01.023>.
12. Zheng, R., Du, J.P., Gao, S., Somekawa, H., Ogata, S., and Tsuji, N. (2020). Transition of dominant deformation mode in bulk polycrystalline pure Mg by ultra-grain refinement down to sub-micrometer. *Acta Mater.* 198, 35–46. <https://doi.org/10.1016/j.actamat.2020.07.055>.
13. Xu, Y., Li, Z., and Duan, W. (2014). Thermal and thermoelectric properties of graphene. *Small* 10, 2182–2199. <https://doi.org/10.1002/smll.201303701>.
14. Tsai, J.L., and Tu, J.F. (2010). Characterizing mechanical properties of graphite using molecular dynamics simulation. *Mater. Des.* 31, 194–199. <https://doi.org/10.1016/j.matdes.2009.06.032>.
15. Inagaki, M., Kaburagi, Y., and Hishiyama, Y. (2014). Thermal management material: graphite. *Adv. Eng. Mater.* 16, 494–506. <https://doi.org/10.1002/adem.201300418>.
16. Li, P., Cao, K., Jiang, C., Xu, S., Gao, L., Xiao, X., and Lu, Y. (2019). In situ tensile fracturing of multilayer graphene nanosheets for their in-plane mechanical properties. *Nanotechnology* 30, 475708. <https://doi.org/10.1088/1361-6528/ab3cd3>.
17. Yang, M., Liu, Y., Fan, T., and Zhang, D. (2020). Metal-graphene interfaces in epitaxial and bulk systems: a review. *Prog. Mater. Sci.* 110, 100652. <https://doi.org/10.1016/j.pmatsci.2020.100652>.
18. Li, J., Zhang, X., and Geng, L. (2019). Effect of heat treatment on interfacial bonding and strengthening efficiency of graphene in GNP/Al composites. *Compos. Appl. Sci. Manuf.* 121, 487–498. <https://doi.org/10.1016/j.compositesa.2019.04.010>.
19. Chu, K., Wang, F., Wang, X.H., Li, Y.B., Geng, Z.R., Huang, D.J., and Zhang, H. (2018). Interface design of graphene/copper composites by matrix alloying with titanium. *Mater. Des.* 144, 290–303. <https://doi.org/10.1016/j.matdes.2018.02.038>.
20. Zhu, Y., Bai, H., Xue, C., Zhou, R., Xu, Q., Tao, P., Wang, C., Wang, J., and Jiang, N. (2016). Thermal conductivity and mechanical properties of a flake graphite/Cu composite with a silicon nano-layer on a graphite surface. *RSC Adv.* 6, 98190–98196. <https://doi.org/10.1039/c6ra17804a>.
21. Xue, C., Bai, H., Tao, P.F., Wang, J.W., Jiang, N., and Wang, S.L. (2016). Thermal conductivity and mechanical properties of flake graphite/Al composite with a SiC nano-layer on graphite surface. *Mater. Des.* 108, 250–258. <https://doi.org/10.1016/j.matdes.2016.06.122>.
22. Chen, J., Ren, S., He, X., and Qu, X. (2017). Properties and microstructure of nickel-coated graphite flakes/copper composites fabricated by spark plasma sintering. *Carbon* 121, 25–34. <https://doi.org/10.1016/j.carbon.2017.05.082>.
23. Bai, H., Xue, C., Lyu, J.L., Li, J., Chen, G.X., Yu, J.H., Lin, C.T., Lv, D.J., and Xiong, L.M. (2018). Thermal conductivity and mechanical properties of flake graphite/copper composite with a boron carbide-boron nano-layer on graphite surface. *Compos. Appl. Sci. Manuf.* 106, 42–51. <https://doi.org/10.1016/j.compositesa.2017.11.019>.
24. Liu, Q., Zhang, C., Cheng, J., Wang, F., Lv, Z., Liu, Y., and Qu, X. (2019). Modeling of interfacial design and thermal conductivity in graphite flake/Cu composites for thermal management applications. *Appl. Therm. Eng.* 156, 351–358. <https://doi.org/10.1016/j.applthermaleng.2019.04.063>.
25. Li, X., Shi, H., Wang, X., Hu, X., Xu, C., and Shao, W. (2022). Direct synthesis and modification of graphene in Mg melt by converting CO₂: a novel route to achieve high strength and stiffness in graphene/Mg composites. *Carbon* 186, 632–643. <https://doi.org/10.1016/j.carbon.2021.10.017>.
26. Chen, L., Zhao, Y., Li, M., Li, L., Hou, L., and Hou, H. (2021). Reinforced AZ91D magnesium alloy with thixomolding process facilitated dispersion of graphene nanoplatelets and enhanced interfacial interactions. *Mater. Sci. Eng., A* 804, 140793. <https://doi.org/10.1016/j.msea.2021.140793>.
27. Hou, J., Du, W., Parande, G., Gupta, M., and Li, S. (2019). Significantly enhancing the strength+ ductility combination of Mg-9Al alloy using multi-walled carbon nanotubes. *J. Alloys Compd.* 790, 974–982. <https://doi.org/10.1016/j.jallcom.2019.03.243>.
28. Ye, J., Li, J., Luo, H., Tan, J., Chen, X., Feng, B., Zheng, K., and Pan, F. (2022). Effect of micron-Ti particles on microstructure and mechanical properties of Mg-3Al-1Zn based composites. *Mater. Sci. Eng., A* 833, 142526. <https://doi.org/10.1016/j.msea.2021.142526>.
29. Parviz, S., Hashemi, S.M., Asgarinia, F., Nematollahi, M., and Elahinia, M. (2021). Effective parameters on the final properties of NiTi-based alloys manufactured by powder metallurgy methods: a review. *Prog. Mater. Sci.* 117, 100739. <https://doi.org/10.1016/j.pmatsci.2020.100739>.
30. Jiang, Q., Zhang, P., Yu, Z., Shi, H., Wu, D., Yan, H., Ye, X., Lu, Q., and Tian, Y. (2021). A review on additive manufacturing of pure copper. *Coatings* 11, 740. <https://doi.org/10.3390/coatings11060740>.
31. Yegyan Kumar, A., Wang, J., Bai, Y., Huxtable, S.T., and Williams, C.B. (2019). Impacts of process-induced porosity on material properties of copper made by binder jetting additive manufacturing. *Mater. Des.* 182, 108001. <https://doi.org/10.1016/j.matdes.2019.108001>.
32. Cao, H., Xiong, D.B., Tan, Z., Fan, G., Li, Z., Guo, Q., Su, Y., Guo, C., and Zhang, D. (2019). Thermal properties of in situ grown graphene reinforced copper matrix laminated composites. *J. Alloys Compd.* 771, 228–237. <https://doi.org/10.1016/j.jallcom.2018.08.274>.
33. Sakamoto, M., Akiyama, S., and Ogi, K. (1997). Suppression of ignition and burning of molten Mg alloys by Ca bearing stable oxide film. *J. Mater. Sci. Lett.* 16, 1048–1050. <https://doi.org/10.1023/A:1018526708423>.
34. Kuai, N., Li, J., Chen, Z., Huang, W., Yuan, J., and Xu, W. (2011). Experiment-based investigations of magnesium dust explosion characteristics. *J. Loss Prev. Process. Ind.* 24, 302–313. <https://doi.org/10.1016/j.jlp.2011.01.006>.
35. Li, J., Zhang, X., Qian, M., Jia, Z., Imran, M., and Geng, L. (2023). Inhibiting GNPs breakage during ball milling for a balanced strength-ductility match in GNPs/Al composites. *Compos. Appl. Sci. Manuf.* 166, 107410. <https://doi.org/10.1016/j.compositesa.2022.107410>.
36. Rohatgi, P.K., Ajay Kumar, P., Chelliah, N.M., and Rajan, T.P.D. (2020). Solidification processing of cast metal matrix composites over the last 50 years and opportunities for the future. *JOM* 72, 2912–2926. <https://doi.org/10.1007/s11837-020-04253-x>.
37. Hashim, J., Looney, L., and Hashmi, M.S.J. (1999). Metal matrix composites: production by the stir casting method. *J. Mater. Process. Technol.* 92–93, 1–7. [https://doi.org/10.1016/S0924-0136\(99\)00118-1](https://doi.org/10.1016/S0924-0136(99)00118-1).
38. Nie, K.B., Wang, X.J., Deng, K.K., Hu, X.S., and Wu, K. (2021). Magnesium matrix composite reinforced by nanoparticles-a review. *Journal of magnesium and alloys* 9, 57–77. <https://doi.org/10.1016/j.jma.2020.08.018>.
39. Pan, H., Pan, F., Yang, R., Peng, J., Zhao, C., She, J., Gao, Z., and Tang, A. (2014). Thermal and electrical conductivity of binary

- magnesium alloys. *J. Mater. Sci.* 49, 3107–3124. <https://doi.org/10.1007/s10853-013-8012-3>.
40. Wang, J., Zhu, G., Wang, L., Vasilev, E., Park, J.S., Sha, G., Zeng, X., and Knezevic, M. (2021). Origins of high ductility exhibited by an extruded magnesium alloy Mg-1.8 Zn-0.2 Ca: experiments and crystal plasticity modeling. *J. Mater. Sci. Technol.* 84, 27–42. <https://doi.org/10.1016/j.jmst.2020.12.047>.
41. Pan, H., Kang, R., Li, J., Xie, H., Zeng, Z., Huang, Q., Yang, C., Ren, Y., and Qin, G. (2020). Mechanistic investigation of a low-alloy Mg-Ca-based extrusion alloy with high strength-ductility synergy. *Acta Mater.* 186, 278–290. <https://doi.org/10.1016/j.actamat.2020.01.017>.
42. Leng, J., Wu, G., Zhou, Q., Dou, Z., and Huang, X. (2008). Mechanical properties of SiC/Gr/Al composites fabricated by squeeze casting technology. *Scr. Mater.* 59, 619–622. <https://doi.org/10.1016/j.scriptamat.2008.05.018>.
43. Li, W.J., Deng, K.K., Zhang, X., Nie, K.B., and Xu, F.J. (2016). Effect of ultra-slow extrusion speed on the microstructure and mechanical properties of Mg-4Zn-0.5 Ca alloy. *Mater. Sci. Eng., A* 677, 367–375. <https://doi.org/10.1016/j.msea.2016.09.059>.
44. Yang, K.M., Ma, Y.C., Zhang, Z.Y., Zhu, J., Sun, Z.B., Chen, J.S., Zhao, H.H., Song, J., Li, Q., Chen, N.Q., et al. (2020). Anisotropic thermal conductivity and associated heat transport mechanism in roll-to-roll graphene reinforced copper matrix composites. *Acta Mater.* 197, 342–354. <https://doi.org/10.1016/j.actamat.2020.07.021>.
45. Wu, G., Yu, Z., Jiang, L., Zhou, C., Deng, G., Deng, X., and Xiao, Y. (2019). A novel method for preparing graphene nanosheets/Al composites by accumulative extrusion-bonding process. *Carbon* 152, 932–945. <https://doi.org/10.1016/j.carbon.2019.06.077>.
46. Zareian, Z., Emamy, M., Malekan, M., Mirzadeh, H., Kim, W.J., and Bahmani, A. (2020). Tailoring the mechanical properties of Mg-Zn magnesium alloy by calcium addition and hot extrusion process. *Mater. Sci. Eng., A* 774, 138929. <https://doi.org/10.1016/j.msea.2020.138929>.
47. Hou, J., Du, W., Wang, Z., Li, S., Liu, K., and Du, X. (2020). Combination of enhanced thermal conductivity and strength of MWCNTs reinforced Mg-6Zn matrix composite. *J. Alloys Compd.* 838, 155573. <https://doi.org/10.1016/j.jallcom.2020.155573>.
48. Du, X., Du, W., Wang, Z., Liu, K., and Li, S. (2021). Simultaneously improved mechanical and thermal properties of Mg-Zn-Zr alloy reinforced by ultra-low content of graphene nanoplatelets. *Appl. Surf. Sci.* 536, 147791. <https://doi.org/10.1016/j.apsusc.2020.147791>.
49. Li, Z.H., Sasaki, T.T., Shiroyama, T., Miura, A., Uchida, K., and Hono, K. (2020). Simultaneous achievement of high thermal conductivity, high strength and formability in Mg-Zn-Ca-Zr sheet alloy. *Mater. Res. Lett.* 8, 335–340. <https://doi.org/10.1080/21663831.2020.1759718>.
50. Yuan, J., Zhang, K., Li, T., Li, X., Li, Y., Ma, M., Luo, P., Luo, G., and Hao, Y. (2012). Anisotropy of thermal conductivity and mechanical properties in Mg-5Zn-1Mn alloy. *Mater. Des.* 40, 257–261. <https://doi.org/10.1016/j.matdes.2012.03.046>.
51. Zhong, L., Peng, J., Li, M., Wang, Y., Lu, Y., and Pan, F. (2016). Effect of Ce addition on the microstructure, thermal conductivity and mechanical properties of Mg-0.5 Mn alloys. *J. Alloys Compd.* 661, 402–410. <https://doi.org/10.1016/j.jallcom.2015.11.107>.
52. Li, B., Hou, L., Wu, R., Zhang, J., Li, X., Zhang, M., Dong, A., and Sun, B. (2017). Microstructure and thermal conductivity of Mg-2Zn-Zr alloy. *J. Alloys Compd.* 722, 772–777. <https://doi.org/10.1016/j.jallcom.2017.06.148>.
53. Liu, Y.F., Jia, X.J., Qiao, X.G., Xu, S.W., and Zheng, M.Y. (2019). Effect of La content on microstructure, thermal conductivity and mechanical properties of Mg-4Al magnesium alloys. *J. Alloys Compd.* 806, 71–78. <https://doi.org/10.1016/j.jallcom.2019.07.267>.
54. Yang, C., Pan, F., Chen, X., Luo, N., Han, B., and Zhou, T. (2018). Thermal conductivity and mechanical properties of Sm-containing Mg-Zn-Zr alloys. *Mater. Sci. Technol.* 34, 138–144. <https://doi.org/10.1080/02670836.2017.1366707>.
55. Li, G., Zhang, J., Wu, R., Feng, Y., Liu, S., Wang, X., Jiao, Y., Yang, Q., and Meng, J. (2018). Development of high mechanical properties and moderate thermal conductivity cast Mg alloy with multiple RE via heat treatment. *J. Mater. Sci. Technol.* 34, 1076–1084. <https://doi.org/10.1016/j.jmst.2017.12.011>.
56. Feng, Y., Zhang, J., Qin, P., Liu, S., Yang, Q., Meng, J., Wu, R., and Xie, J. (2019). Characterization of elevated-temperature high strength and decent thermal conductivity extruded Mg-Er-Y-Zn alloy containing nano-spaced stacking faults. *Mater. Charact.* 155, 109823. <https://doi.org/10.1016/j.matchar.2019.109823>.
57. Zhang, B., Jia, H., Lian, Q., Jiang, L., and Wu, G. (2019). Effect of extrusion treatment on mechanical, thermal conductivity and corrosion resistance of magnesium alloys. *mat. express* 9, 405–412. <https://doi.org/10.1166/mex.2019.1514>.
58. Li, H., Zong, H., Li, S., Jin, S., Chen, Y., Cabral, M.J., Chen, B., Huang, Q., Chen, Y., Ren, Y., et al. (2022). Uniting tensile ductility with ultrahigh strength via composition undulation. *Nature* 604, 273–279. <https://doi.org/10.1038/s41586-022-04459-w>.
59. Zhou, C., Huang, W., Chen, Z., Ji, G., Wang, M.L., Chen, D., and Wang, H.W. (2015). In-plane thermal enhancement behaviors of Al matrix composites with oriented graphite flake alignment. *Compos. B Eng.* 70, 256–262. <https://doi.org/10.1016/j.compositesb.2014.11.018>.
60. Mouder, J.F., Stickle, W.F., Sobol, P.E., and Bomben, K.E. (2011). *Handbook of X-Ray Photoelectron Spectroscopy* (Perkin-Elmer Corporation).
61. Shin, S.E., Choi, H.J., Hwang, J.Y., and Bae, D.H. (2015). Strengthening behavior of carbon/metal nanocomposites. *Sci. Rep.* 5, 16114–16117. <https://doi.org/10.1038/srep16114>.
62. Olsson, E., Hussain, T., Karton, A., and Cai, Q. (2020). The adsorption and migration behavior of divalent metals (Mg, Ca, and Zn) on pristine and defective graphene. *Carbon* 163, 276–287. <https://doi.org/10.1016/j.carbon.2020.03.028>.
63. Datta, D., Li, J., and Shenoy, V.B. (2014). Defective graphene as a high-capacity anode material for Na-and Ca-ion batteries. *ACS Appl. Mater. Interfaces* 6, 1788–1795. <https://doi.org/10.1021/am404788e>.
64. Shamsuddin, M.; TMS (2016). *Physical Chemistry of Metallurgical Processes* (Wiley, TMS).
65. Knacke, O., and Hesselmann, K. (1991). *Thermochemical Properties of Inorganic Substances* (Springer).
66. Sun, Z., Luo, S., Qi, P., and Fan, L.S. (2012). Ionic diffusion through Calcite (CaCO_3) layer during the reaction of CaO and CO_2 . *Chem. Eng. Sci.* 81, 164–168. <https://doi.org/10.1016/j.ces.2012.05.042>.
67. Anderson, T.F. (1969). Self-diffusion of carbon and oxygen in calcite by isotope exchange with carbon dioxide. *J. Geophys. Res.* 74, 3918–3932. <https://doi.org/10.1029/JB074i015p03918>.
68. Tamankar, S.S., and Doraiswamy, L.K. (1979). Analysis of solid-solid reactions: a review. *AIChE J.* 25, 561–582. <https://doi.org/10.1002/aic.690250402>.
69. Delannay, F., Froyen, L., and Deruyttere, A. (1987). The wetting of solids by molten metals and its relation to the preparation of metal-matrix composites. *J. Mater. Sci.* 22, 1–16. <https://doi.org/10.1007/BF01160545>.
70. Laha, T., Kuchibhatla, S., Seal, S., Li, W., and Agarwal, A. (2007). Interfacial phenomena in thermally sprayed multiwalled carbon nanotube reinforced aluminum nanocomposite. *Acta Mater.* 55, 1059–1066. <https://doi.org/10.1016/j.actamat.2006.09.025>.
71. Qiu, D., and Zhang, M.X. (2014). The nucleation crystallography and wettability of Mg grains on active Al_2Y inoculants in an Mg-10 wt% Y Alloy. *J. Alloys Compd.* 586, 39–44. <https://doi.org/10.1016/j.jallcom.2013.10.042>.
72. Lu, K. (2016). Stabilizing nanostructures in metals using grain and twin boundary architectures. *Nat. Rev. Mater.* 1, 16019. <https://doi.org/10.1038/natrevmats.2016.19>.
73. Abrahamson, J. (1973). The surface energies of graphite. *Carbon* 11, 337–362. [https://doi.org/10.1016/0008-6223\(73\)90075-4](https://doi.org/10.1016/0008-6223(73)90075-4).

74. Xiao, S., Edwards, S.A., and Gräter, F. (2011). A new transferable forcefield for simulating the mechanics of CaCO₃ crystals. *J. Phys. Chem. C* 115, 20067–20075. <https://doi.org/10.1021/jp202743v>.
75. Li, Z., Wang, H., Guo, Q., Li, Z., Xiong, D.B., Su, Y., Gao, H., Li, X., and Zhang, D. (2018). Regain strain-hardening in high-strength metals by nanofiller incorporation at grain boundaries. *Nano Lett.* 18, 6255–6264. <https://doi.org/10.1021/acs.nanolett.8b02375>.
76. Zhang, N., and Chen, Y. (2013). Nanoscale plastic deformation mechanism in single crystal aragonite. *J. Mater. Sci.* 48, 785–796. <https://doi.org/10.1007/s10853-012-6796-1>.
77. Nieto, A., Bisht, A., Lahiri, D., Zhang, C., and Agarwal, A. (2017). Graphene reinforced metal and ceramic matrix composites: a review. *Int. Mater. Rev.* 62, 241–302. <https://doi.org/10.1080/09506608.2016.1219481>.
78. Fukuda, H., and Chou, T.W. (1982). A probabilistic theory of the strength of short-fibre composites with variable fibre length and orientation. *J. Mater. Sci.* 17, 1003–1011. <https://doi.org/10.1007/BF00543519>.
79. Guo, X., Wang, L., Wang, M., Qin, J., Zhang, D., and Lu, W. (2012). Effects of degree of deformation on the microstructure, mechanical properties and texture of hybrid-reinforced titanium matrix composites. *Acta Mater.* 60, 2656–2667. <https://doi.org/10.1016/j.actamat.2012.01.032>.
80. Pan, H., Qin, G., Huang, Y., Ren, Y., Sha, X., Han, X., Liu, Z.Q., Li, C., Wu, X., Chen, H., et al. (2018). Development of low-alloyed and rare-earth-free magnesium alloys having ultra-high strength. *Acta Mater.* 149, 350–363. <https://doi.org/10.1016/j.actamat.2018.03.002>.
81. Tan, Z., Li, Z., Xiong, D.B., Fan, G., Ji, G., and Zhang, D. (2014). A predictive model for interfacial thermal conductance in surface metallized diamond aluminum matrix composites. *Mater. Des.* 55, 257–262. <https://doi.org/10.1016/j.matdes.2013.09.060>.
82. Swartz, E.T., and Pohl, R.O. (1989). Thermal boundary resistance. *Rev. Mod. Phys.* 61, 605–668. <https://doi.org/10.1103/RevModPhys.61.605>.
83. Momenzadeh, L., Moghtaderi, B., Buzzi, O., Liu, X., Sloan, S.W., and Murch, G.E. (2018). The thermal conductivity decomposition of calcite calculated by molecular dynamics simulation. *Comput. Mater. Sci.* 141, 170–179. <https://doi.org/10.1016/j.commatsci.2017.09.033>.
84. Gillet, P., McMillan, P., Schott, J., Badro, J., and Grzechnik, A. (1996). Thermodynamic properties and isotopic fractionation of calcite from vibrational spectroscopy of ¹⁸O-substituted calcite. *Geochim. Cosmochim. Acta* 60, 3471–3485. [https://doi.org/10.1016/0016-7037\(96\)00178-0](https://doi.org/10.1016/0016-7037(96)00178-0).
85. Han, Z., and Fina, A. (2011). Thermal conductivity of carbon nanotubes and their polymer nanocomposites: a review. *Prog. Polym. Sci.* 36, 914–944. <https://doi.org/10.1016/j.progpolymsci.2010.11.004>.

STAR★METHODS

KEY RESOURCES TABLE

REAGENT or RESOURCE	SOURCE	IDENTIFIER
Chemicals, peptides, and recombinant proteins		
Pure Mg (99%)	Shanxi Wenxi Yinguang Magnesium Industry (Group) Co., Ltd.	CAS: 7439-95-4
Pure Zn (99.99%)	Aladdin	CAS: 7440-66-6
Pure Ca (99.5%)	Aladdin	CAS: 7440-70-2
Ultrathin graphite flakes (98%)	Qingdao Weijie Graphite Co. Ltd.	CAS: 12751-41-6
Oxalate acid (AR)	China National Pharmaceutical Group Shanxi Co., Ltd.	CAS: 144-62-7
Nitric acid (AR)	China National Pharmaceutical Group Shanxi Co., Ltd.	CAS: 7697-37-2
Acetic acid (AR)	China National Pharmaceutical Group Shanxi Co., Ltd.	CAS: 64-19-7

RESOURCE AVAILABILITY

Lead contact

Further information and requests for resources and reagents should be directed to and will be fulfilled by the lead contact, Kun-Kun Deng (dengkunkun@tyut.edu.cn).

Materials availability

This study did not generate new unique reagents. All chemicals were obtained from commercial resources and used as received.

Data and code availability

- The published article includes all datasets generated or analyzed during this study.
- This paper does not report original code. Crystal data of CaCO_3 (aragonite) and MgZn_2 intermetallic are available in the Crystallography Open Database (<http://www.Crystallography.net/cod/search.html>) under COD ID: 2100187 and 5910078, respectively.
- Any additional information required to reanalyze the data reported in this paper is available from the [lead contact](#) upon request.
- All data reported in this paper will be shared by the [lead contact](#) upon request.

EXPERIMENTAL MODEL AND SUBJECT DETAILS

This study does not use experimental methods typical in the life sciences.

METHOD DETAILS

Material fabrication

The matrix alloy Mg-5Zn-0.5Ca (wt.%), named as ZX50, was prepared from pure Mg (99%), pure Zn (99.9%), and pure Ca (99.5%). The raw ultrathin graphite flakes (UGFs) were purchased from Qingdao Weijie Graphite Co. Ltd. (P.R. China) which was exfoliated from nature squama graphite. The UGFs/ZX50 composites with volume fractions of 1%, 2% and 3% were fabricated in this work. The volume fraction of added UGFs can be converted into weight percent, by:

$$M_{Gr} = \frac{V_f}{1 - V_f} \frac{\rho_{Gr}}{\rho_m} M_m \quad (\text{Equation M1})$$

where V_f is the volume fraction, M_{Gr} and M_m are the weight of graphite and Mg alloy, respectively. The ρ_{Gr} and ρ_m are the density of graphite and Mg alloy, respectively.

A certain weight of UGFs was preheated at 400°C for 1h, and then added into the ZX50 semi-solid melt which was stirred at 620°C. Afterwards, the melt was reheated to 720°C, and ultrasonically processed for 15 min with a power of ~2.0 KW and a frequency of ~20 kHz. Then the composite melt was poured into

a steel mold preheated at 400°C and solidified under a pressure of 125 MPa. The whole process was protected by anti-oxidizing gas atmosphere (1 vol.% SF₆ + 99 vol.% CO₂).

The as-cast ingots were homogenized at 430°C for 16 h, and then extruded at 210°C with extrusion ratio of 16:1 at a constant ram speed of 0.1 mm/s. Eventually, the rods of 10 mm in diameter were obtained following extrusion.

Microstructure analysis

Microstructures were observed by optical microscopy (OM, OLYMPUS GX53) and scanning electron microscope (SEM, HITACHI SU8010) equipped with an energy-dispersive X-ray spectroscopy (EDS) analysis system. The specimens of as-extruded alloy and composites were etched in mixed acid (1g oxalate + 1ml HNO₃ + 1ml acetic acid + 150ml distilled water). The average grain size (\bar{d}) and volume fraction (VF_{DRX}) of DRXed grains were measured by Image-Pro plus 5.0 software. The microstructures were further characterized with transmission electron microscopy (TEM, JEM-2100F). TEM samples were prepared by mechanical polishing combined with ion beam thinning (Gatan PIPS, Model 695). Phase components and lattice analysis were conducted from the diffraction profiles measured by the X-ray diffraction (XRD, Rigaku Ultima IV) with Cu K α radiation ($k=1.5406\text{\AA}$). X-ray photoelectron spectroscopy (XPS, ThermoFischer, ESCALAB 250Xi with an Al K α ($h\nu=1486.6\text{eV}$) X-ray source) was used to measure the bonding characteristics of the interface. Raman spectroscopy (Renishaw inVia) measurements with a 532 nm Ar+ laser at ambient temperature were carried out to validate the feature of UGFs.

Thermal conductivity and mechanical property test

Thermal conductivity K (W/(m·K)) was obtained via the following equation (Ref. 3):

$$K = \alpha\rho C_p \quad (\text{Equation M2})$$

where α is thermal diffusivity (m²/s), ρ is density (g/cm³) and C_p is specific heat capacity [J/(g·K)]. The thermal diffusivity was measured by laser flash method (Netzsch LFA 447) at 25°C. The specific heat capacity at 25°C was measured using differential scanning calorimeter (DSC, TA Q20). The measurements were carried out with a heating rate of 10°C·min⁻¹ in a nitrogen atmosphere, with a flow rate of 50 mL·min⁻¹. The NIST synthetic sapphire, SRM 720, was used as a reference material. The room temperature density of the materials was obtained from a densimeter (JHY 120F) using Archimedes method. Samples for the thermal diffusivity were machined from extruded bars with the heat transfer direction along the extrusion direction. The tensile specimens with gauge length of 25 mm and cross-sectional areas of 6 mm × 2 mm were machined from the extruded rods with loading axis parallel to the extruding direction. The tensile tests were performed at room temperature using an Exceed model E45 test machine at a tensile rate of 0.5 mm/min.

QUANTIFICATION AND STATISTICAL ANALYSIS

This study does not include statistical analysis or quantification.